J. Fluid Mech. (2024), *vol*. 999, A103, doi:10.1017/jfm.2024.989

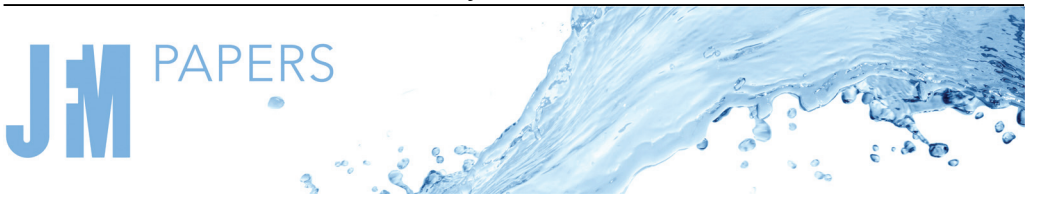

Vapour bubbles produced by long-pulsed laser: a race between advection and phase transition

Xuning Zhao[1], Wentao Ma[1], Junqin Chen[2], Gaoming Xiang[2,3,4], Pei Zhong[2] and Kevin Wang[1,†]

[1]Kevin T. Crofton Department of Aerospace and Ocean Engineering, Virginia Tech, Blacksburg, VA 24061, USA

[2]Thomas Lord Department of Mechanical Engineering and Materials Science, Duke University, Durham, NC 27708, USA

[3]Optics and Thermal Radiation Research Center, Institute of Frontier and Interdisciplinary Science, Shandong University, Qingdao 266237, PR China

[4]School of Energy and Power Engineering, Shandong University, Jinan, Shandong 250061, PR China

(Received 31 August 2023; revised 5 September 2024; accepted 3 October 2024)

Vapour bubbles produced by long-pulsed laser often have complex non-spherical shapes that reflect some characteristics of the laser beam. The transition between two commonly observed shapes, namely, a rounded pear-like shape and an elongated conical shape, is studied using a new computational model that combines compressible multiphase fluid dynamics with laser radiation and phase transition. Two laboratory experiments are simulated, in which a holmium:YAG or thulium fibre laser is used to generate bubbles of different shapes. In both cases, the predicted bubble nucleation and morphology agree reasonably well with the experimental observation. The full-field results of laser irradiance, temperature, velocity and pressure are analysed to explain bubble dynamics and energy transmission. It is found that due to the lasting energy input, the vapour bubble's dynamics is driven not only by advection, but also by the continued vaporisation at its surface. Vaporisation lasts less than 1 μs in the case of the pear-shaped bubble, compared with over 50 μs for the elongated bubble. It is thus hypothesised that the bubble's morphology is determined by competition. When the speed of advection is higher than that of vaporisation, the bubble tends to grow spherically. Otherwise, it elongates along the laser beam direction. To test this hypothesis, the two speeds are defined analytically using a model problem, then estimated for the experiments using simulation results. The results

† Email address for correspondence: kevinwgy@vt.edu

support the hypothesis. They also suggest that when the laser's power is fixed, a higher laser absorption coefficient and a narrower beam facilitate bubble elongation.

Key words: boiling, bubble dynamics, cavitation

1. Introduction

Vapour bubbles appear in many scientific studies and real-world applications that involve laser radiation. To researchers who study cavitation and bubble dynamics, laser is a convenient tool to create bubbles at a precise location without too much disturbance to the surrounding environment (Brujan *et al.* 2001; Tomita *et al.* 2002; Zwaan *et al.* 2007). To technology developers and practitioners who use high-power laser in a liquid environment, cavitation is often an inevitable phenomenon and the resulting vapour bubbles may have both beneficial and detrimental effects. Example applications in this regard include liquid-assisted laser processing (e.g. underwater laser cutting (Chida *et al.* 2003) and laser cleaning (Song *et al.* 2004; Ohl *et al.* 2006)), ocular laser surgery (Vogel *et al.* 1986; Požar 2020), laser angioplasty (Vogel *et al.* 1996) and laser lithotripsy (Fried & Irby 2018; Ho *et al.* 2021). The most common effects of laser-induced cavitation include the creation of a vapour channel, the disturbance of the local flow field, a propulsive force from bubble expansion, and material damages caused by the shock waves and microjets from bubble collapse (Dijkink & Ohl 2008; Mohammadzadeh, Mercado & Ohl 2015; Chen *et al.* 2022; Xiang *et al.* 2023). Improving a technology often requires optimising the trade-offs between different effects.

While laser-induced cavitation can be roughly described as localised phase change due to radiation, the detailed physics involves laser emission and absorption, phase transition and the dynamics and thermodynamics of a two-phase fluid flow. Within this multiphysics problem, a key external (i.e. user-specified) parameter is the duration of the laser pulse. In different applications, the value of this parameter varies from femtoseconds (10^{-15} s) to more than 1 second (Juhasz *et al.* 1996; Zwaan *et al.* 2007; Ho *et al.* 2021). For example, nanosecond pulsed lasers are widely used in experiments of cavitation studies (Zwaan *et al.* 2007), microsecond pulsed lasers are common in laser lithotripsy operations (Ho *et al.* 2021) and lasers with millisecond duration are utilised in underwater laser cutting experiments (Jain *et al.* 2010; Choubey *et al.* 2015).

When the pulse duration is much smaller than the acoustic time scale in the fluid medium (i.e. characteristic length divided by sound speed), the laser energy input is referred to as short-pulsed. Typically, the laser energy is absorbed by the medium through nonlinear processes, leading to intense light absorption and cascading ionisation in the medium. This process results in the formation of a plasma bubble, commonly referred to as optical breakdown (Schoppink *et al.* 2023). In this case, laser radiation can be assumed to be a preceding event that ends before the bubble starts to expand. Therefore, the analysis of fluid and bubble dynamics can be separated from that of laser radiation (Byun & Kwak 2004; Zein, Hantke & Warnecke 2013; Koch *et al.* 2016; Zhang & Prosperetti 2021). In this paper, we study cavitation induced by long-pulsed laser, which means the duration of the laser pulse is longer than the acoustic time scale, yet shorter than the thermal diffusion time in the fluid. Unlike short-pulsed lasers, heating in this scenario occurs through linear absorption, leading to localised liquid–vapour phase transition, known as thermocavitation (Padilla-Martinez *et al.* 2014). In this case, laser radiation and phase transition may continue after the formation of the initial bubble. The assumption mentioned above is no

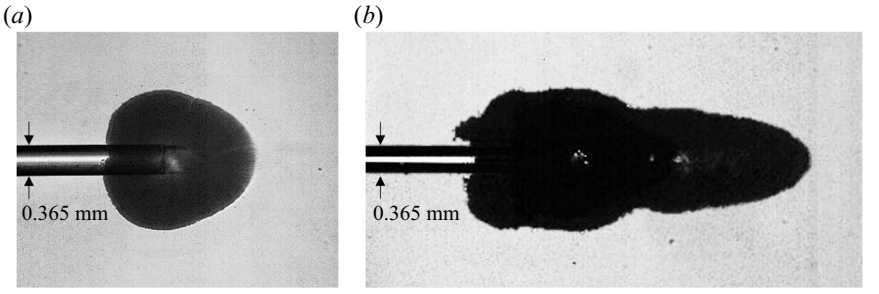

Figure 1. Non-spherical vapour bubbles generated by long-pulsed laser. (*a*) A rounded, pear-shaped bubble generated by Ho:YAG laser with wavelength 2080 nm, pulse energy 0.2 J, pulse duration 70 μs and acoustic time scale (fibre diameter divided by sound speed) 0.25 μs. (*b*) An elongated bubble generated by thulium fibre laser with wavelength 1940 nm, pulse energy 0.11 J, pulse duration 170 μs and acoustic time scale 0.25 μs.

longer valid. Laser radiation, phase transition and the fluid dynamics and thermodynamics are now interdependent. They need to be analysed together.

The vapour bubbles generated by long-pulsed laser often have a non-spherical shape that reflects some characteristics of the laser beam, such as its direction and width. Figure 1 shows two commonly observed shapes that will be studied in this paper, namely a rounded pear-like shape and an elongated conical shape. Depending on the application, one or the other may be preferred. For example, a rounded bubble, when it collapses, is more likely to generate a strong liquid jet that damages a surrounding material (Chen *et al.* 2022; Xiang *et al.* 2023). An elongated bubble, on the other hand, can be more energy efficient in creating a long vapour channel that allows laser to pass through. While bubbles of both shapes have been observed in many experiments (Mohammadzadeh *et al.* 2015; Hardy *et al.* 2016; Fried & Irby 2018; Xiang *et al.* 2023), elucidating the formation mechanisms of non-spherical shapes remains challenging. Moreover, the causal relation between bubble morphology and laser setting (e.g. wavelength, power magnitude and distribution, pulse duration and diverging angle) is still unclear. Many fundamental questions of practical significance are unresolved, such as the following.

(i) Does phase transition (vaporisation) last for a substantial period of time or does it occur instantaneously?
(ii) What fraction of the laser energy input is used to create the vapour bubble?
(iii) How can we control the laser setting so that the vapour bubble has a desired shape?

It is difficult to answer these questions by laboratory experiment only. While the evolution of bubble shape can be measured by high-speed optical imaging, measurement of the pressure, velocity and temperature fields inside and around the vapour bubble is challenging (Dular & Coutier-Delgosha 2013; Khlifa *et al.* 2013; Petkovšek & Dular 2013). Such limitations hinder the possibility to predict the time span of phase changes and to provide detailed explanations for bubble dynamics. The literature does offer studies on bubble shape transitions, including the relationship between bubble morphology and laser pulse duration (Asshauer, Rink & Delacretaz 1994; Jansen *et al.* 1996), as well as the influence of pulse energy (Ho *et al.* 2021). However, the experimental constraints impede a comprehensive exploration of the link between laser parameters and bubble geometry. For example, some parameters of laser (e.g. wavelength) cannot be varied continuously in experiments. Therefore, the partition of energy and the cause of the bubble's shape change cannot be determined easily. In this work, we combine laboratory experiment with numerical simulation to study long-pulsed laser-induced cavitation, focusing on the

physics behind pear-shaped and elongated bubbles. We try to investigate the causal relation between the laser's parameters and the vapour bubble's shape, and to gain some insight on the three open questions mentioned previously.

In this work, we adopt a new computational model that combines compressible multiphase fluid dynamics with laser radiation and phase transition. In the past, bubble dynamics simulations were typically based on the solution of Rayleigh–Plesset, boundary integral or multi-dimensional Navier–Stokes equations (Plesset & Prosperetti 1977; Klaseboer *et al.* 2006; Warnez & Johnsen 2015; Wang 2017; Cao *et al.* 2021*a*). A simulation usually starts with one or multiple spherical bubbles as the initial condition. In most cases, the initial state inside each bubble is set to a constant. Although there are studies focused on simulating bubble dynamics induced by lasers, they tend to decouple the laser radiation and vaporisation process from bubble dynamics. The phase transition due to laser exposure is modelled separately to determine the constant initial states inside the bubble. This approach can be justified for bubbles generated by short-pulsed laser, given that radiation and vaporisation both complete at a smaller time scale compared with that of fluid dynamics. For long-pulsed laser-induced cavitation, the same approach is no longer valid. It would not be able to predict the effects of the lasting energy input, such as the possible continuation of phase transition and the formation of non-spherical bubbles. In this work, we couple the multiphase compressible inviscid Navier–Stokes equations with a laser radiation equation that models the absorption of laser energy by the fluid flow. The laser radiation equation is obtained by customising the radiative transfer equation (RTE) using the special properties of laser, including monochromaticity, directionality and a measurable (often non-zero) focusing or diverging angle. The fundamental components of the computational framework include an embedded boundary method that allows the solution of laser and fluid governing equations on the same mesh, a method of latent heat reservoir for vaporisation prediction, a local level set method for interface tracking and the FIVER (FInite Volume method with Exact multi-material Riemann solvers) method to enforce interface conditions. The algorithms and properties of this framework were published recently together with some verification tests (Zhao, Ma & Wang 2023). The FIVER method by itself is the pivot of a body of literature that includes simulation method development, verification and validation, and various applications in aerospace, ocean and biomedical engineering (see Farhat, Gerbeau & Rallu (2012), Main *et al.* (2017), Ma *et al.* (2023), Islam *et al.* (2023), Huang, De Santis & Farhat (2018) and the references therein). Compared with the physical model presented in Zhao *et al.* (2023), a few improvements are made in this work, such as the inclusion of heat diffusion and the modelling of laser fibre using an embedded boundary method.

In two separate laboratory experiments, we use a holmium:yttrium–aluminum–garnet (Ho:YAG) laser and thulium fibre laser (TFL) to generate a pear-shaped bubble and an elongated bubble. In both cases, the bubble dynamics is recorded by high-speed optical imaging. In addition, the temporal profile of laser power is measured using a photodetector. These experimental measurements are treated as ground truth in this study. We simulate the two experiments using the computational model described previously. The measured laser power profile is used as an input to each simulation, which starts with a single phase (liquid water) in the entire computational domain. The simulations are capable of predicting bubble nucleation due to laser radiation. They provide transient, full-field results of laser irradiance, temperature, pressure, velocity and density. They also track the dynamics of the vapour bubble using a level set function. To validate the computational model, we compare the bubble dynamics predicted by the simulations with

the high-speed images obtained from the experiments. Then, we analyse the full-field simulation results to explain the bubble dynamics and energy transmission. Based on the results, we hypothesise that the bubble's shape is determined by a race between advection and phase transition. At any time instant, if the speed of advection is higher than that of vaporisation, the bubble tends to grow spherically. Otherwise, it tends to elongate along the laser beam direction. To clarify this hypothesis, we build a simplified model problem for which the aforementioned two speeds can be defined analytically. Then, we test the hypothesis using our simulation results. This analytical definition of growth velocities forms a bridge between laser parameters and bubble morphology, providing guidance for the manipulation of laser settings to achieve targeted bubble shapes.

The remainder of this paper is organised as follows. Section 2 describes the physical model adopted in this study, including governing equations, constitutive models, and a phase transition model. Section 3 provides a summary of the numerical methods used to solve the model equations. In §§ 4 and 5, we present the experimental and simulation results for a pear-shaped bubble and an elongated bubble. In § 6, we discuss the transition between these two different shapes. Finally, § 7 provides a summary of this study and some concluding remarks.

2. Physical model

2.1. *Fluid dynamics and thermodynamics*

Figure 2 illustrates the problem investigated in this paper, showing a test case that generates a pear-shaped vapour bubble. The computational analysis is designed to start at the time when laser is just activated. At this time, the fluid domain is occupied completely by liquid water. The analysis is expected to predict the localised water vaporisation due to laser radiation, the subsequent bubble and fluid dynamics, and the dissipation of laser energy in this two-phase fluid medium. Therefore, we solve the following compressible inviscid Navier–Stokes equations that include radiative heat transfer, applied to both liquid and vapour phases:

$$\frac{\partial \boldsymbol{W}(\boldsymbol{x}, t)}{\partial t} + \boldsymbol{\nabla} \cdot \mathcal{F}(\boldsymbol{W}) = \boldsymbol{\nabla} \cdot \mathcal{G}(\boldsymbol{W}), \quad \forall \boldsymbol{x} \in \Omega = \Omega_0 \cup \Omega_1, \quad t > 0, \tag{2.1}$$

with

$$\boldsymbol{W} = \begin{bmatrix} \rho \\ \rho \boldsymbol{V} \\ \rho e_t \end{bmatrix}, \quad \mathcal{F} = \begin{bmatrix} \rho \boldsymbol{V}^{\mathrm{T}} \\ \rho \boldsymbol{V} \otimes \boldsymbol{V} + p\boldsymbol{I} \\ (\rho e_t + p)\boldsymbol{V}^{\mathrm{T}} \end{bmatrix}, \quad \mathcal{G} = \begin{bmatrix} \boldsymbol{0}^{\mathrm{T}} \\ \boldsymbol{0} \\ (k\boldsymbol{\nabla} T - \boldsymbol{q}_r)^{\mathrm{T}} \end{bmatrix}. \tag{2.2a–c}$$

Here, $\Omega \subset \mathbb{R}^3$ denotes the domain of the fluid flow. Open subsets Ω_0 and Ω_1 represent the subdomains occupied by the liquid and vapour phases, respectively. They are time-dependent. In our experiments, a sharp boundary between the liquid and vapour phases can be clearly captured by high-speed imaging. Therefore, we assume $\Omega_0 \cap \Omega_1 = \emptyset$. Here ρ, $\boldsymbol{V}$, p and T denote the fluid's density, velocity, pressure and temperature, respectively, and e_t is the total energy per unit mass, given by

$$e_t = e + \tfrac{1}{2}|\boldsymbol{V}|^2, \tag{2.3}$$

where e denotes the fluid's internal energy per unit mass, k is the thermal conductivity coefficient, which takes different values in Ω_0 and Ω_1, and $\boldsymbol{q}_r$ denotes the radiative heat flux induced by laser. Equation (2.1) can be viewed as a generalisation of classical

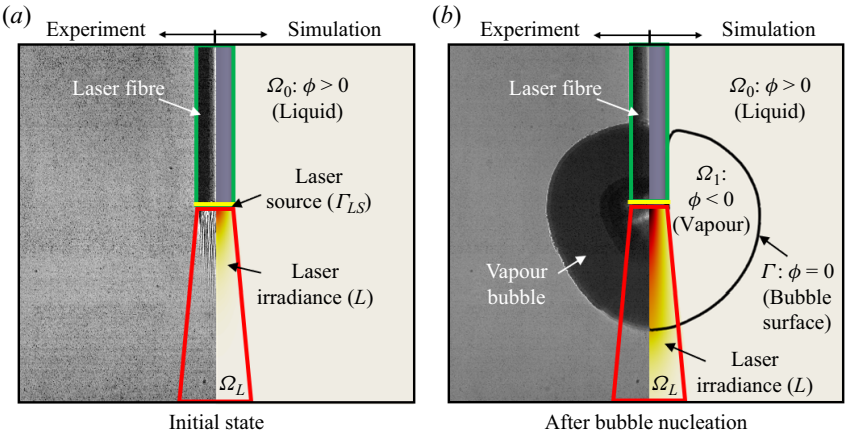

Figure 2. Long-pulse laser-induced vaporisation and bubble expansion: an example problem.

models for spherical bubbles (Plesset & Prosperetti 1977; Prosperetti & Plesset 1978). For example, the heat equation in Prosperetti & Plesset (1978) can be derived from the energy conservation equation in (2.1) by assuming an incompressible flow, spherical symmetry, a linear temperature equation and absence of radiative heating.

Equation (2.1) needs to be closed by a complete equation of state (EOS) for each phase. The computational model and solver utilised in this study supports arbitrary convex EOS (Ma *et al.* 2023). In this study, we adopt the Noble–Abel stiffened-gas equation (Le Métayer & Saurel 2016) for both phases. Specifically,

$$p_{\mathcal{I}}(\rho, e) = (\gamma_{\mathcal{I}} - 1)\frac{e - q_{\mathcal{I}}}{\dfrac{1}{\rho} - b_{\mathcal{I}}} - \gamma_{\mathcal{I}} p_{c\mathcal{I}}, \tag{2.4}$$

in which the subscript $\mathcal{I} \in \{0, 1\}$ identifies the liquid (0) and vapour (1) phases. For each phase, γ, p_c, q and b are constant parameters that characterise its thermodynamic properties. For example, a non-zero b allows the model to have a variable Grüneisen parameter that depends on ρ. Clearly, (2.4) is a generalisation of perfect-gas, stiffened-gas and Noble–Abel EOSs (Le Métayer & Saurel 2016).

For a given pressure equation such as (2.4), the choice of temperature equation is not unique. We adopt that proposed by Le Métayer & Saurel (2016), i.e.

$$T_{\mathcal{I}}(\rho, e) = \frac{1}{c_{v\mathcal{I}}}\left(e - q_{\mathcal{I}} - \left(\frac{1}{\rho} - b_{\mathcal{I}}\right) p_{c\mathcal{I}}\right), \tag{2.5}$$

where c_v denotes the specific heat capacity at constant volume, assumed to be a constant. It can be shown that the specific heat capacity at constant pressure, c_p, is also a constant, given by $c_p = \gamma c_v$. Combining (2.4) and (2.5) gives a complete EOS that satisfies the first law of thermodynamics.

Two groups of EOS parameter values are tested in this study, as shown in table 1. Neither of them was calibrated specifically for laser-induced cavitation (see Zein, Hantke & Warnecke 2013; Le Métayer & Saurel 2016). We show in § 4 that the simulation result is indeed influenced by these parameter values.

Group	Reference	Phase	γ	p_c (Pa)	c_v (J (kg K)$^{-1}$)	b (m^3 kg^{-1})	q (J kg^{-1})
1	Zein *et al.* (2013)	Liquid	2.057	1.066×10^9	3.449×10^3	0	-1994.674×10^3
		Vapour	1.327	0	1.2×10^3	0	1995×10^3
2	Le Métayer & Saurel (2016)	Liquid	1.19	7.028×10^8	4.285×10^3	6.61×10^{-4}	-1177.788×10^3
		Vapour	1.47	0	0.955×10^3	0	2077.616×10^3

Table 1. Noble–Abel stiffened gas EOS parameters for water.

2.2. *Liquid–vapour interface*

We model the bubble surface as a sharp interface with zero thickness. It is defined by

$$\Gamma = \partial\Omega_0 \cap \partial\Omega_1. \tag{2.6}$$

On the interface, we assume continuity of normal velocity and pressure, i.e.

$$\begin{gathered}\left(\lim_{\boldsymbol{x}'\to\boldsymbol{x},\boldsymbol{x}'\in\Omega_0} \boldsymbol{V}(\boldsymbol{x}',t) - \lim_{\boldsymbol{x}'\to\boldsymbol{x},\ \boldsymbol{x}'\in\Omega_1} \boldsymbol{V}(\boldsymbol{x}',t)\right)\cdot\boldsymbol{n}(\boldsymbol{x},t) = 0,\\ \lim_{\boldsymbol{x}'\to\boldsymbol{x},\ \boldsymbol{x}'\in\Omega_0} p(\boldsymbol{x}',t) = \lim_{\boldsymbol{x}'\to\boldsymbol{x},\ \boldsymbol{x}'\in\Omega_1} p(\boldsymbol{x}',t),\end{gathered} \qquad \forall \boldsymbol{x}\in\Gamma, \quad t\geq 0, \tag{2.7}$$

where $\boldsymbol{n}$ denotes the normal to Γ.

Here Γ is time-dependent, and must be solved for during the analysis. We represent it implicitly as the zero level set of a signed distance function, ϕ, defined in the closure of Ω. That is,

$$\Gamma(t) = \{\boldsymbol{x}\in\bar{\Omega},\ \phi(\boldsymbol{x},t) = 0\}, \tag{2.8}$$

where $\bar{\Omega}$ denotes the closure of Ω.

In this way, the aforementioned phase identifier, $\mathcal{I}$, is given by

$$\mathcal{I}(\boldsymbol{x},t) = \begin{cases} 0, & \text{if } \phi(\boldsymbol{x},t) > 0\},\\ 1, & \text{if } \phi(\boldsymbol{x},t) < 0\}. \end{cases} \tag{2.9}$$

The evolution of Γ in time is driven by both phase transition and advection. The advection of Γ by the fluid flow is governed by the level-set equation,

$$\frac{\partial\phi}{\partial t} + \boldsymbol{V}\cdot\nabla\phi = 0, \tag{2.10}$$

where $\boldsymbol{V}$ is the flow velocity due to advection.

At the beginning of the analysis, $\Omega = \Omega_0$, and $\Gamma = \emptyset$. Therefore, we initialise ϕ to be a constant positive value everywhere in the domain, and start solving (2.10) only after phase transition starts. The detection and handling of laser-induced phase transition are discussed in § 2.4.

2.3. *Laser radiation*

Following Zhao *et al.* (2023), $\Omega_L \subset \Omega$ denotes the region in the fluid domain that is exposed to laser. The laser generators used in this study have a flat surface with a small

diverging angle. Therefore, Ω_L is in the shape of a truncated cone (figure 2, also see Zhao *et al.* 2023). Within Ω_L, energy conservation implies

$$\nabla \cdot (\mathcal{L}\hat{\boldsymbol{s}}) = \mu_\alpha(\eta)\mathcal{L}_b(\boldsymbol{x}, \eta) - \mu_\alpha(\eta)\mathcal{L}(\boldsymbol{x}, \hat{\boldsymbol{s}}, \eta) - \mu_s(\eta)\mathcal{L}(\boldsymbol{x}, \hat{\boldsymbol{s}}, \eta) + \frac{\mu_s(\eta)}{4\pi}\int_{4\pi} \mathcal{L}(\boldsymbol{x}, \hat{\boldsymbol{s}}_{\boldsymbol{i}}, \eta)\Phi(\hat{\boldsymbol{s}}_{\boldsymbol{i}}, \hat{\boldsymbol{s}})\,\mathrm{d}\hat{\boldsymbol{s}}_i, \tag{2.11}$$

where $\mathcal{L} = \mathcal{L}(\boldsymbol{x}, \hat{\boldsymbol{s}}, \eta)$ denotes the spectral radiance (dimensions: [mass][time]$^{-3}$ [length]$^{-1}$) at position $\boldsymbol{x} \in \mathbb{R}^3$, along direction $\hat{\boldsymbol{s}}$, at wavelength η. Here μ_α and μ_s denote the coefficients of absorption and scattering, respectively. They depend on the laser's wavelength and the medium. We use $\mathcal{L}_b$ to denote the blackbody radiance and $\Phi(\hat{\boldsymbol{s}}_{\boldsymbol{i}}, \hat{\boldsymbol{s}})$ to denote the scattering phase function, which gives the probability that a ray from one direction $\hat{\boldsymbol{s}}_{\boldsymbol{i}}$ would be scattered into another direction $\hat{\boldsymbol{s}}$. If $\hat{\boldsymbol{s}}$ is independent of $\boldsymbol{x}$, the left-hand side of (2.11) simplifies to $\nabla\mathcal{L} \cdot \boldsymbol{s}$, which gives the well-known RTE (Modest 2013; Howell *et al.* 2020).

The radiative heat flux $\boldsymbol{q}_r$ in (2.1) is obtained by integrating $\mathcal{L}$ over all directions and the interval of relevant wavelengths, (η_{min}, η_{max}). That is,

$$\boldsymbol{q}_{\boldsymbol{r}}(\boldsymbol{x}) = \int_{\eta_{min}}^{\eta_{max}} \int_{4\pi} \mathcal{L}(\boldsymbol{x}, \hat{\boldsymbol{s}}, \eta)\hat{\boldsymbol{s}}\,\mathrm{d}\hat{\boldsymbol{s}}\,\mathrm{d}\eta. \tag{2.12}$$

The special properties of laser light allow us to simplify (2.11) and (2.12). The intensity of the laser light is much higher than the blackbody radiance. Therefore, we assume

$$\mathcal{L}_b(\boldsymbol{x}, \eta) = 0. \tag{2.13}$$

In addition, $\mathcal{L}$ is non-zero only along the direction of laser propagation ($\boldsymbol{s}$) and at the fixed laser wavelength. That is,

$$\mathcal{L}(\boldsymbol{x}, \hat{\boldsymbol{s}}, \eta) = L(\boldsymbol{x})\delta(\hat{\boldsymbol{s}} - \boldsymbol{s})\delta(\eta - \eta_0), \tag{2.14}$$

where $\delta(\cdot)$ denotes the delta function, and the variable $L(\boldsymbol{x})$ on the right-hand side is irradiance (dimensions: [mass][time]$^{-3}$). With these assumptions, a laser radiation equation is obtained by substituting (2.14) and (2.13) into (2.11), i.e.

$$\nabla \cdot (L\boldsymbol{s}) = \nabla L \cdot \boldsymbol{s} + (\nabla \cdot \boldsymbol{s})L = -\mu_\alpha L. \tag{2.15}$$

For a diverging beam,

$$\boldsymbol{s}(\boldsymbol{x}) = \frac{\boldsymbol{x} - \boldsymbol{x}_a}{|\boldsymbol{x} - \boldsymbol{x}_a|}, \tag{2.16}$$

where $\boldsymbol{x}_a$ denotes the focal point of the beam. Then, substituting (2.14) into (2.12) yields

$$\boldsymbol{q}_r = L\boldsymbol{s}. \tag{2.17}$$

In this study, we measure the time history of laser power, $P_0(t)$, in laboratory experiments. We assume the laser irradiance on the surface of the laser fibre (i.e. Γ_{LS} in figure 2) follows a Gaussian distribution, also known as a Gaussian beam (Welch & Van Gemert 2011). Therefore, on Γ_{LS} we have

$$L(\boldsymbol{x}, t) = \frac{2P_0(t)}{\pi w_0^2}\exp\left(\frac{-2|\boldsymbol{x} - \boldsymbol{x}_0|^2}{w_0^2}\right), \tag{2.18}$$

where $\boldsymbol{x}_0$ denotes the centre of Γ_{LS}, w_0 is the waist radius and $P_0(t)$ is the time-dependent laser power function, which is adjusted from measured laboratory data to account for the finite domain of the Gaussian function.

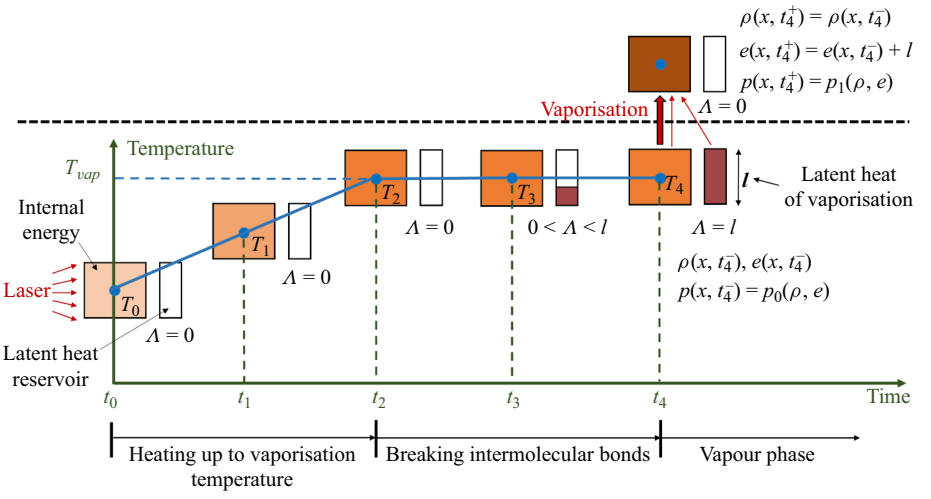

Figure 3. Predicting laser-induced vaporisation by the method of latent heat reservoir.

2.4. *Vaporisation*

We employ the method of latent heat reservoir proposed in Zhao *et al.* (2023) to predict laser-induced vaporisation. As shown in figure 3, the fundamental idea of this method is to introduce a new variable, $\Lambda(\boldsymbol{x}, t)$, to track the intermolecular potential energy in the liquid phase. The vaporisation temperature, T_{vap}, and latent heat, l, are assumed to be constant and used in the method as coefficients. When the analysis starts, $\Lambda(\boldsymbol{x}, t)$ is initialised to 0 everywhere. As the liquid absorbs laser energy, temperature increases gradually. At any point $\boldsymbol{x} \in \Omega_0$, once T_{vap} is reached, additional heat, due to radiation, advection or diffusion, is added to Λ. When Λ reaches l, phase transition occurs. The accumulated heat represented by Λ is released and subsequently added to the internal energy of the vapour phase. In figure 3, this time instant is denoted by t_4. We assume that phase transition completes instantaneously at each point in the domain through an isochoric process. The state variables before and after phase transition are related by

$$\mathcal{I}^+ = 1, \quad \text{(i.e. vapour)} \tag{2.19}$$

$$\rho^+ = \rho^-, \tag{2.20}$$

$$e^+ = e^- + \Lambda^-, \tag{2.21}$$

$$\Lambda^+ = 0, \tag{2.22}$$

$$\phi^+ = -\frac{\Delta x}{2}, \tag{2.23}$$

where the superscripts $-$ and $+$ indicate the variable's value before and after phase transition, e.g.

$$\rho^+ \equiv \lim_{\substack{t \to t_4 \\ t > t_4}} \rho(\boldsymbol{x}, t). \tag{2.24}$$

In (2.23), Δx denotes the local element size in the computational mesh. The pressure and temperature after phase transition are obtained naturally from the EOS of the vapour

phase, i.e.

$$p^+ = p_1(\rho^+, e^+), \tag{2.25}$$

$$T^+ = T_1(\rho^+, e^+). \tag{2.26}$$

The pressure rise, $p^+ - p^-$, drives the expansion of the vapour bubble.

At each time step, if phase transition occurs, the level set function ϕ is restored to a signed distance function by solving the reinitialisation equation,

$$\frac{\partial \phi}{\partial \tilde{t}} + S(\phi_0)(|\nabla \phi| - 1) = 0, \tag{2.27}$$

to the steady state. Here, $\tilde{t}$ is a fictitious time variable, ϕ_0 is the level set function before reinitialisation and $S(\phi_0)$ is a smoothed sign function, given by

$$S(\phi_0) = \frac{\phi_0}{\sqrt{\phi_0^2 + \varepsilon^2}}, \tag{2.28}$$

where ε is a constant coefficient, set to the minimum element size of the mesh. The steady-state solution of (2.27) is then used as the new initial condition to integrate the level set equation (2.10) forwards in time.

3. Numerical methods

3.1. *FIVER (FInite Volume method based on Exact multiphase Riemann problem solvers)*

We apply a recently developed laser–fluid computational framework to solve the above model equations (Zhao *et al.* 2023). The fluid governing equations are semi-discretised using a fixed, non-interface conforming finite-volume mesh, denoted by Ω^h (figure 4). The laser fibre is modelled as a fixed slip wall, and the associated boundary condition is enforced using an embedded boundary method (Wang 2017; Cao, Main & Wang 2018; Cao *et al.* 2021*a*; Cao, Wang & Wang 2021*b*). Therefore, Ω^h also covers the region occupied by the laser fibre. Around each node $\boldsymbol{n}_i \in \Omega^h$, a control volume C_i is created. Applying the standard finite-volume spatial discretisation to (2.1) yields

$$\frac{\partial \boldsymbol{W}_i}{\partial t} + \frac{1}{|C_i|} \sum_{j \in Nei(i)} \int_{\partial C_{ij}} \mathcal{F}(\boldsymbol{W}) \cdot \boldsymbol{n}_{ij} \, \mathrm{d}S = \frac{1}{|C_i|} \int_{C_i} \nabla \cdot \mathcal{G}(\boldsymbol{W}) \, \mathrm{d}\boldsymbol{x}, \tag{3.1}$$

where $\boldsymbol{W}_i$ denotes the average value of $\boldsymbol{W}$ in C_i, $Nei(i)$ denotes the set of nodes connected to node $\boldsymbol{n}_i$, $\partial C_{ij} = \partial C_i \cap \partial C_j$, $\boldsymbol{n}_{ij}$ is the unit normal to ∂C_{ij} and $|C_i|$ denotes the volume of C_i.

The FIVER method is used to calculate the advective flux across each facet ∂C_{ij}. Depending on the locations of nodes $\boldsymbol{n}_i$ and $\boldsymbol{n}_j$, there are four different cases.

(i) If $\boldsymbol{n}_i$ and $\boldsymbol{n}_j$ belong to the same phase subdomain (Ω_0 or Ω_1), the conventional monotonic upstream-centred scheme for conservation laws (MUSCL) is used to compute the flux across ∂C_{ij}, i.e.

$$F_{ij} = \|\partial C_{ij}\| \Phi(\boldsymbol{W}_{ij}, \boldsymbol{W}_{ji}, \boldsymbol{n}_{ij}, \mathrm{EOS}^{(i)}) = -F_{ji}, \tag{3.2}$$

where $\|\partial C_{ij}\|$ is the area of ∂C_{ij}, $\boldsymbol{W}_{ij}$ and $\boldsymbol{W}_{ji}$ denote the reconstructed state variables on the two sides of ∂C_{ij} and Φ represents the numerical flux function. In this work,

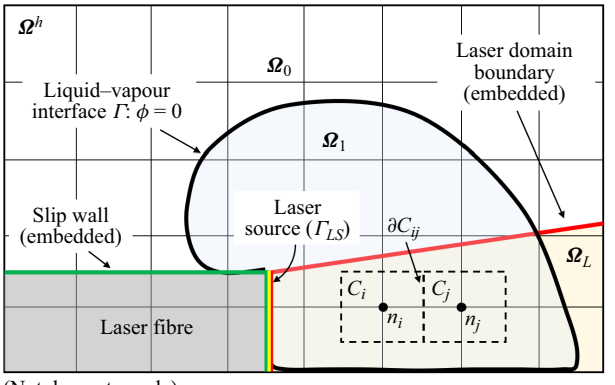

(Not drawn to scale)

Figure 4. Finite-volume discretisation of the spatial domain.

the local Lax–Friedrichs flux function is employed. Here F_{ij} and F_{ji} are used to update the state variables within control volumes C_i and C_j, respectively.

(ii) If $\boldsymbol{n}_i$ and $\boldsymbol{n}_j$ belong to different phase subdomains, a one-dimensional (1-D) bimaterial Riemann problem is constructed along the edge between $\boldsymbol{n}_i$ and $\boldsymbol{n}_j$, i.e.

$$\frac{\partial \boldsymbol{w}}{\partial \tau} + \frac{\partial \mathcal{F}(\boldsymbol{w})}{\partial \xi} = 0, \quad \text{with } \boldsymbol{w}(\xi, 0) = \begin{cases} \boldsymbol{w}_i, & \text{if } \xi \le 0, \\ \boldsymbol{w}_j, & \text{if } \xi > 0, \end{cases} \tag{3.3}$$

where τ denotes the time coordinate and ξ denotes the spatial coordinate along the axis aligned with $\boldsymbol{n}_{ij}$ and centred at the phase interface between $\boldsymbol{n}_i$ and $\boldsymbol{n}_j$. The initial states $\boldsymbol{w}_i$ and $\boldsymbol{w}_j$ are the projections of $\boldsymbol{W}_i$ and $\boldsymbol{W}_j$ on the ξ axis. This 1-D two-phase compressible flow problem can be solved exactly (Ma *et al.* 2023). The solution is self-similar, and satisfies the interface conditions (2.7). The state variables on the i- and j-sides of the interface, denoted by $\boldsymbol{W}_{ij}^*$ and $\boldsymbol{W}_{ji}^*$, are substituted into the same numerical flux function Φ. Specifically,

$$F_{ij} = \|\partial C_{ij}\| \Phi(\boldsymbol{W}_{ij}, \boldsymbol{W}_{ij}^*, \boldsymbol{n}_{ij}, \mathrm{EOS}^{(i)}), \tag{3.4}$$

$$F_{ji} = \|\partial C_{ij}\| \Phi(\boldsymbol{W}_{ji}, \boldsymbol{W}_{ji}^*, \boldsymbol{n}_{ij}, \mathrm{EOS}^{(j)}). \tag{3.5}$$

(iii) If one of $\boldsymbol{n}_i$ and $\boldsymbol{n}_j$ belongs to a fluid-phase subdomain (Ω_0 or Ω_1), whereas the other is covered by the laser fibre, a 1-D half-Riemann problem is constructed and solved exactly (Wang 2017; Cao *et al.* 2021*a*). The solution at the wall boundary is used to compute the advective fluxes across ∂C_{ij}, similar to the previous case.

(iv) If both $\boldsymbol{n}_i$ and $\boldsymbol{n}_j$ are covered by the laser fibre, the flux across ∂C_{ij} is set to zero.

Details of FIVER can be found in previous papers such as Farhat *et al.* (2012) and Main *et al.* (2017). It is noteworthy that this method is not strictly conservative, mainly for two reasons (Main *et al.* 2017). First, the flux balance $F_{ij} + F_{ji} = 0$ typically does not hold when $\boldsymbol{n}_i$ and $\boldsymbol{n}_j$ are in different phase subdomains. Second, when the material interface crosses one node due to advection, the state variables within the corresponding control volume are updated either by extrapolation or using the Riemann solution, both of which lead to a loss of conservation.

3.2. *Diffusive heat fluxes*

The right-hand side of (3.1) includes two parts, namely the heat diffusion term ($\int_{C_i} \nabla \cdot (k\nabla T)\,\mathrm{d}\boldsymbol{x}$) and the radiation term ($\int_{C_i} \nabla \cdot \boldsymbol{q}_r\,\mathrm{d}\boldsymbol{x}$). The heat diffusion term is evaluated using a finite-volume method, i.e.

$$\int_{C_i} \nabla \cdot (k\nabla T)\,\mathrm{d}\boldsymbol{x} = \int_{\partial C_{ij}} (k\nabla T) \cdot \boldsymbol{n}_{ij}\,\mathrm{d}S = \sum_{j\in Nei(i)} (k\nabla T)_{ij} A_{ij} \cdot \boldsymbol{n}_{ij}, \tag{3.6}$$

where A_{ij} is the area of facet ∂C_{ij} and $(k\nabla T)_{ij} \cdot \boldsymbol{n}_{ij}$ denotes the heat flow due to diffusion that crosses the facet ∂C_{ij}. In this work, it is computed by

$$(k\nabla T)_{ij} \cdot \boldsymbol{n}_{ij} = k_{ij} \frac{T_i - T_j}{\|\boldsymbol{x}_i - \boldsymbol{x}_j\|_2}, \tag{3.7}$$

with

$$k_{ij} = \frac{2k_i k_j}{k_i + k_j}. \tag{3.8}$$

Here, k_i and k_j denote the thermal conductivity at nodes $\boldsymbol{n}_i$ and $\boldsymbol{n}_j$, specifically. We assume that the liquid–vapour interface is isothermal, and it can be shown that if $\boldsymbol{n}_i$ and $\boldsymbol{n}_j$ belong to different phase subdomains, (3.7) and (3.8) enforce energy balance at the interface, with interface temperature (Faghri & Zhang 2006)

$$T_{ij} = \frac{k_i T_i + k_j T_j}{k_i + k_j}. \tag{3.9}$$

We set the thermal conductivity at all the nodes covered by the laser fibre to zero. In this way, (3.7) and (3.8) enforce the adiabatic boundary condition at the surface of the laser fibre.

3.3. *Laser radiation and laser–fluid coupling*

The radiation term is evaluated by

$$\int_{C_i} (\nabla \cdot \boldsymbol{q}_r)\,\mathrm{d}\boldsymbol{x} = (\nabla \cdot \boldsymbol{q}_r)_i |C_i|. \tag{3.10}$$

At each time step, the divergence of the radiative flux, $\nabla \cdot \boldsymbol{q}_r$, is computed using the current solution of the laser radiation equation (2.15). In this work, the laser radiation equation is discretised using the same finite-volume mesh (Ω^h) created for the fluid governing equations (figure 4). Specifically, integrating (2.15) within an arbitrary cell C_i yields

$$\sum_{j\in Nei(i)} A_{ij} L_{ij} (\boldsymbol{s}_{ij} \cdot \boldsymbol{n}_{ij}) = -|C_i| \mu_\alpha(T_i) L_i, \tag{3.11}$$

where L_i is the cell average of L within C_i. Here $\boldsymbol{s}_{ij}$ represents the laser direction at ∂C_{ij}. It is set to the laser direction at the midpoint between nodes $\boldsymbol{n}_i$ and $\boldsymbol{n}_j$ and is calculated

by (2.16). L_{ij} is the value of L at facet ∂C_{ij}. In this work, it is evaluated by the mean flux method, i.e.

$$L_{ij} = \begin{cases} \alpha L_i + (1-\alpha)L_j & \text{if } \boldsymbol{s}_{ij} \cdot n_{ij} \geq 0, \\ (1-\alpha)L_i + \alpha L_j & \text{if } \boldsymbol{s}_{ij} \cdot n_{ij} < 0, \end{cases} \tag{3.12}$$

where $\alpha \in [0.5, 1]$ is a numerical parameter. Substituting (3.12) into (3.11) yields a system of linear equations with the cell averages of laser irradiance as unknowns. The Gauss–Seidel method is applied to solve this system to get L_i.

Notably, the fluid mesh Ω^h does not contain a subset of nodes, edges and elements that resolve the boundary of Ω_L or the laser propagation directions $\boldsymbol{s}(\boldsymbol{x})$. To address this issue, the embedded boundary method proposed in Zhao *et al.* (2023) is adopted in this work. This method involves the population of ghost nodes outside the side boundary of the laser domain using second-order mirroring and interpolation techniques.

After solving the laser radiation equation, $\nabla \cdot \boldsymbol{q}_r$ in (3.10) is obtained by

$$(\nabla \cdot \boldsymbol{q}_r)_i = \nabla \cdot (L_i \boldsymbol{s}) = -\mu_\alpha(T_i) L_i, \tag{3.13}$$

and then added to (3.1).

3.4. *Vaporisation model implementation*

The method of latent heat reservoir described in § 2.4 is implemented numerically to predict vaporisation. At the end of each time step, for each control volume C_i in Ω_0, the liquid temperature T_i is obtained from (2.5) and compared with T_{vap}. If $T_i > T_{vap}$, we reduce T_i to T_{vap}, and move the excessive heat to the latent heat reservoir, Λ_i. In this case, we update the state variables as follows:

$$T_i = T_{vap}, \tag{3.14}$$

$$\Lambda_i = \Lambda_i + (e_i - e_{vap}), \tag{3.15}$$

$$e_i = e_i - (e_i - e_{vap}) = e_{vap}, \tag{3.16}$$

where e_{vap} denotes the internal energy corresponding to T_{vap}, that is, the solution of (2.5) with $\mathcal{I} = 0$ (liquid), $\rho = \rho_i$ and $T_{\mathcal{I}} = T_{vap}$.

If $T_i \leq T_{vap}$, this means the fluid material within control volume C_i is still below (or exactly equal to) the vaporisation temperature. If $\Lambda_i = 0$, nothing needs to be done. Because of flow advection, it may happen that $\Lambda_i > 0$. In this case, the latent heat stored in the control volume is used to increase the local temperature up to T_{vap}. Specifically, we set

$$\Lambda_i = \Lambda_i - \min(e_{vap} - e_i, \Lambda_i), \tag{3.17}$$

$$e_i = e_i + \min(e_{vap} - e_i, \Lambda_i), \tag{3.18}$$

$$T_i = T_{\mathcal{I}}(\rho_i, e_i), \quad \mathcal{I} = 0. \tag{3.19}$$

Following these operations, we compare Λ_i and l to determine if vaporisation should occur in C_i. If $\Lambda_i \geq l$, this control volume undergoes phase transition, and the fluid state is updated according to (2.19)–(2.26).

The numerical methods described above are implemented in the open-source M2C solver (Wang *et al.* 2021), which is used to run the simulations reported in this paper. Several verification studies can be found in Islam *et al.* (2023), Zhao *et al.* (2023), Cao *et al.* (2021*a*) and earlier papers cited therein. An outline of the solution procedure within

each time step is provided as follows. For simplicity, the forward Euler method is assumed here for time integration. In the actual simulations presented in this paper, a second-order Runge–Kutta method is used.

Input: Numerical solution at t^n: $\boldsymbol{W}^n$, $\mathcal{I}^n$, ϕ^n, L^n and Λ^n.
(1) Compute the residual of the Navier–Stokes equations (3.1).
  (1.1) Compute the advective fluxes (§ 3.1).
  (1.2) Compute the diffusive heat fluxes (3.6).
  (1.3) Compute the radiative heat source (3.10).
(2) Advance the fluid state by one time step $\Rightarrow$ $\boldsymbol{W}^{n+1}$, Λ^{n+1}. Apply boundary conditions.
(3) Compute the residual of the level set equation (2.10).
(4) Advance the level set function by one time step $\Rightarrow$ ϕ^{n+1}. Apply boundary conditions.
(5) Update phase identifier using $\phi^{n+1} \Rightarrow \mathcal{I}^{n+1}$. Update fluid state ($\boldsymbol{W}^{n+1}$, Λ^{n+1}) at nodes that changed phase due to interface motion.
(6) Check for phase transition (§§ 2.4 and 3.4). Update W^{n+1}, Λ^{n+1}, $\mathcal{I}^{n+1}$, and ϕ^{n+1} at nodes that have undergone phase transition (2.19)–(2.26).
(7) If phase transition occurred, reinitialise the level set (2.27).
(8) Solve the laser radiation equation for L^{n+1} (3.11).
Output: Numerical solution at t^{n+1}: $\boldsymbol{W}^{n+1}$, $\mathcal{I}^{n+1}$, ϕ^{n+1}, L^{n+1}, and Λ^{n+1}.

4. A pear-shaped bubble

We employ the computational framework described previously to simulate a laboratory experiment that generates a pear-shaped bubble. The key parameters of the simulation, including laser fibre diameter, laser absorption coefficient and the divergence angle of the laser beam, are set to match the set-up of the experiment. The laser power used in the simulation (i.e. $P_0(t)$ in (2.18)) is determined by fitting the laser power profile measured in the experiment. The simulation's output includes the time histories of the density, temperature, pressure, velocity and laser irradiance fields of the two-phase flow, and the level-set function that tracks the liquid–vapour interface. The bubble's nucleation and evolution are compared with high-speed optical images obtained from the experiment. By analysing the full-field results obtained from the simulation, we try to investigate the causal relation between the laser setting and the bubble's shape.

4.1. *Comparison of experimental and numerical results*

4.1.1. *Laboratory experiment*

In this experiment, a commercial Ho:YAG laser lithotripter (H Solvo 35-W laser, Dornier MedTech, Munich, Germany) with a wavelength of 2080 nm is used to generate the vapour bubble. It is operated at the energy level of 0.2 J with a pulse duration of 70 μs, measured at full width at half maximum. It is clearly a long-pulsed laser, as the acoustic time scale is less than 1 μs. Figure 5(*a*) shows a schematic representation of the experimental set-up. To facilitate the delivery of the pulsed laser, an optical fibre (Dornier SingleFlex 400, Munich, Germany, numerical aperture 0.26) with a core diameter of 0.365 mm is used. The fibre directs laser into a transparent acrylic container (150 mm × 150 mm × 300 mm) filled with degassed water. During the experiment, a series of high-speed images are captured

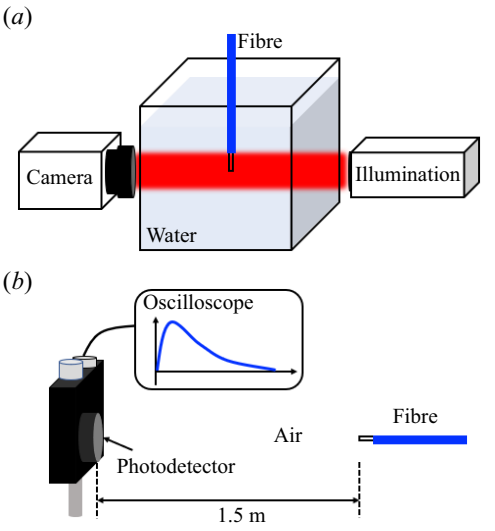

Figure 5. Schematic representation of the experimental set-up for laser-induced cavitation. (*a*) Set-up for capturing the bubble dynamics and (*b*) set-up for measuring the temporal profile of laser power.

using an ultrahigh-speed camera. To enable direct shadowgraph imaging, a 10-ns pulsed laser system (SI-LUX-640, Specialised Imaging) provides the required illumination.

To measure the laser power profile, an additional procedure is conducted in air. The laser pulse is directed towards a photodetector (PDA10D, Thorlabs, Newton, NJ) positioned at a distance of 1.5 m, as illustrated in figure 5(*b*). The photodetector converts the received light into an electronic signal, which is displayed on an oscilloscope. Since air has minimal absorption of laser energy, the recorded data can be considered a reliable indication of the laser power output from the laser fibre when generating the vapour bubble in the bulk fluid.

Figure 6(*a*) presents the time history of the laser power measurement. The laser power increases from the beginning and reaches the maximum at approximately 17 µs. After that, it gradually drops to zero. The graph reveals some fluctuations, which are attributed to measurement noise. Integrating the measured laser power in time yields a total pulse energy of 0.2 J, which is in good agreement with the specified energy level. Figure 6(*b*) presents a series of high-speed images that show the nucleation and evolution of a vapour bubble at the tip of the laser fibre. In the initial stages (at 5 µs), observable streaks emanate from the fibre tip. This phenomenon may arise due to the imperfect Gaussian distribution of the spatial profile of the Ho:YAG laser, characterised by fluctuations (Blackmon, Irby & Fried 2010; Traxer & Keller 2020). These fluctuations result in multiple hot spots, causing non-uniform superheating of the liquid beneath the fibre, which displays as streaks from the side view. The bubble becomes visible at 15 µs. It expands continuously, eventually acquiring a pear-like shape. The bubble maintains cylindrical symmetry about the central axis of the laser beam. However, it is not spherical, unlike the bubbles obtained from previous experiments that use short-pulsed lasers (e.g. Brujan *et al.* 2001; Lauterborn & Vogel 2013; Zhong *et al.* 2020).

Using the measured laser power profile, we can estimate the time it takes to heat water near the laser fibre tip to the vaporisation temperature, T_{vap}. Here, we assume $T_{vap} =$ 373.15 K. We define a cylindrical region next to the laser fibre tip, with a diameter of 0.365 mm (the laser fibre diameter) and a small depth of 0.1 mm. The energy required to raise water temperature in this region from the room temperature (assumed to be 293.15 K)

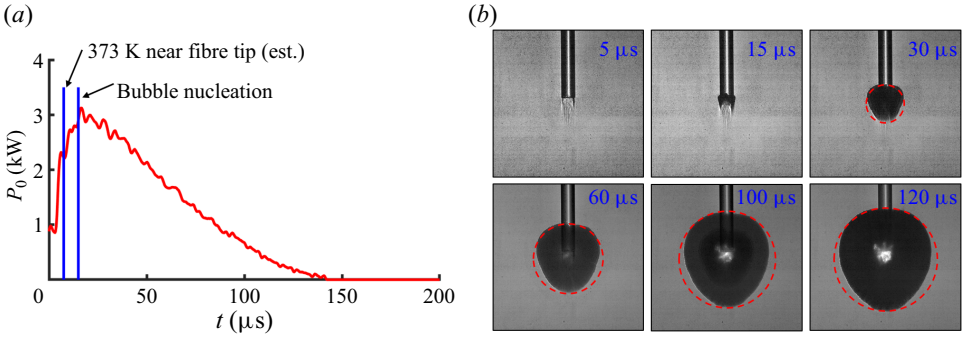

Figure 6. Experimental results obtained with a Ho:YAG laser: (*a*) laser pulse profile measured in air and (*b*) dynamics of the vapour bubble in the bulk fluid. Perfect circles are drawn in (*b*) to show that the vapour bubble is not spherical.

to T_{vap} can be estimated by

$$\Delta E = c_v \Delta T \rho V \approx 0.003 \text{ J}, \tag{4.1}$$

with $c_v = 4.285 \times 10^3$ J (kg K)$^{-1}$ and $\Delta T = 80$ K. The percentage of laser energy absorbed in this region can be roughly estimated by the Beer–Lambert law, which is the one-dimensional version of (2.15). That is,

$$\frac{\partial L}{\partial x} = -\mu_\alpha L. \tag{4.2}$$

The solution of this equation is simply $L(x) = L_0 \exp(-\mu_\alpha x)$, where L_0 denotes the laser irradiance at the source (i.e. $x = 0$). Setting $\mu_\alpha = 2.42$ mm^{-1} for the Ho:YAG laser (Fried & Irby 2018), we find that approximately 21.5 % of the laser energy is absorbed within the depth of the cylindrical region defined previously. Now, by integrating the measured laser power profile (figure 6*a*), we can estimate that at approximately 9 μs, the temperature within the small cylindrical region reaches T_{vap}. From the high-speed images, the vapour bubble does not appear until 15 μs. This finding implies a clear delay in bubble nucleation, which can be attributed to the high latent heat of water.

4.1.2. *Numerical simulation*

Figure 7 shows the set-up of the simulation. A cylindrical domain with a radius of 12 mm and a length of 24 mm is adopted. It is initially occupied by liquid water with density $\rho_0 = 0.001$ g mm^{-3}, velocity $v_0 = 0$ mm s^{-1}, pressure $p_0 = 100$ kPa and temperature $T_0 = 293.15$ K. A far-field boundary condition, ensuring that outgoing waves do not reflect back, is applied to the domain boundaries.

The laser source is positioned at $x = -0.5$ mm, as shown in figure 7(*b*). The laser fibre is modelled as a rigid structure, embedded in the computational domain. It has a radius $r = 0.1825$ mm, consistent with the laboratory experiment. The spatial profile of laser irradiance on the source plane is specified as a Gaussian function (2.18) with waist radius $w_0 = 0.165$ mm, as shown in figure 7(*c*). This value is calibrated based on references indicating a beam diameter of approximately 0.3 mm for the Ho:YAG laser (Fried 2018). The temporal profile of laser power (P_0 in (2.18)) is specified as the blue line shown in figure 7(*d*). It is obtained by fitting the experimental measurement using fast Fourier transform (FFT). The pulse shape is approximately a triangle, with the power growing from 0 to 2.98 kW within 24 μs, then vanishing gradually within 136 μs. The laser

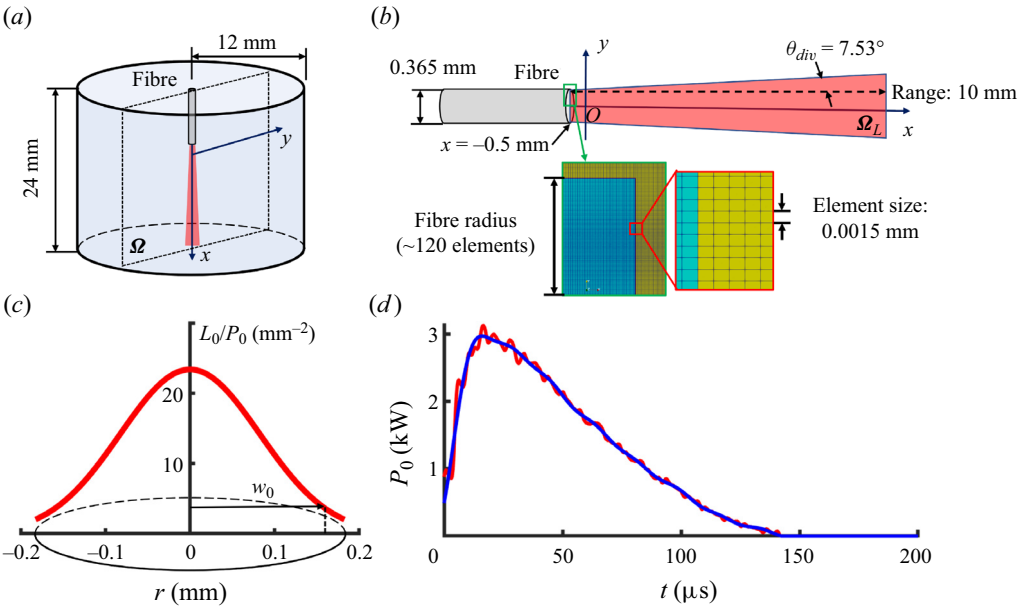

Figure 7. Vapour bubble generated by a Ho:YAG laser: simulation set-up. (*a*) Spatial domain with cylindrical symmetry. (*b*) Geometry of the laser radiation domain and mesh resolution. (*c*) Spatial profile of laser irradiance on the laser source plane. (*d*) Temporal profile of laser power.

beam propagates in the x direction with a divergence angle $\theta_{div} = 7.53^\circ$. Along the beam direction, the length of the laser radiation domain (Ω_L) is set to 10 mm. This length is large enough such that at the far end, laser irradiance is close to zero. The laser absorption coefficient, μ_α, is set to 2.42 mm^{-1} for liquid water (Fried & Irby 2018) and 0.001 mm^{-1} for the vapour. The vaporisation temperature and latent heat of vaporisation are set by $T_{vap} = 373.15$ K and $l = 2256.4$ J g^{-1}, respectively.

The Noble–Abel stiffened-gas EOS (2.4) is employed to model both liquid water and water vapour. First, we adopt the EOS parameters presented in Zein *et al.* (2013), which are listed as Group 1 in table 1. The thermal conductivity, k, is set to 5.576×10^{-4} W (mm K)$^{-1}$ for liquid water and 2.457×10^{-5} W (mm K)$^{-1}$ (Wagner *et al.* 2010) for the vapour.

By the assumption of cylindrical symmetry, we solve the fluid governing equations on a two-dimensional mesh, while adding source terms to the equations to enforce the symmetry (see e.g. Islam *et al.* 2023). The mesh has approximately 2.4 million rectangular elements. In the most refined area, the characteristic element size is about 1.5×10^{-3} mm (as illustrated in figure 7*b*). To put this into context, the diameter of the laser fibre is resolved by about 240 elements. This mesh, chosen after a mesh convergence analysis, provides the appropriate resolution necessary for accurate results. The local level set method with a bandwidth of six elements on each side of the interface is used to track the vapour bubble. Both the fluid governing equations and the level set equation are integrated in time using a second-order Runge–Kutta method. The time step size is approximately 4×10^{-4} μs. The simulation is terminated at $t = 120$ μs, which roughly covers the bubble nucleation and expansion stage observed in the laboratory experiment.

The simulation also generates a pear-shaped bubble, as observed in the experiment. Figure 8 presents a detailed comparison between the experimental data and the

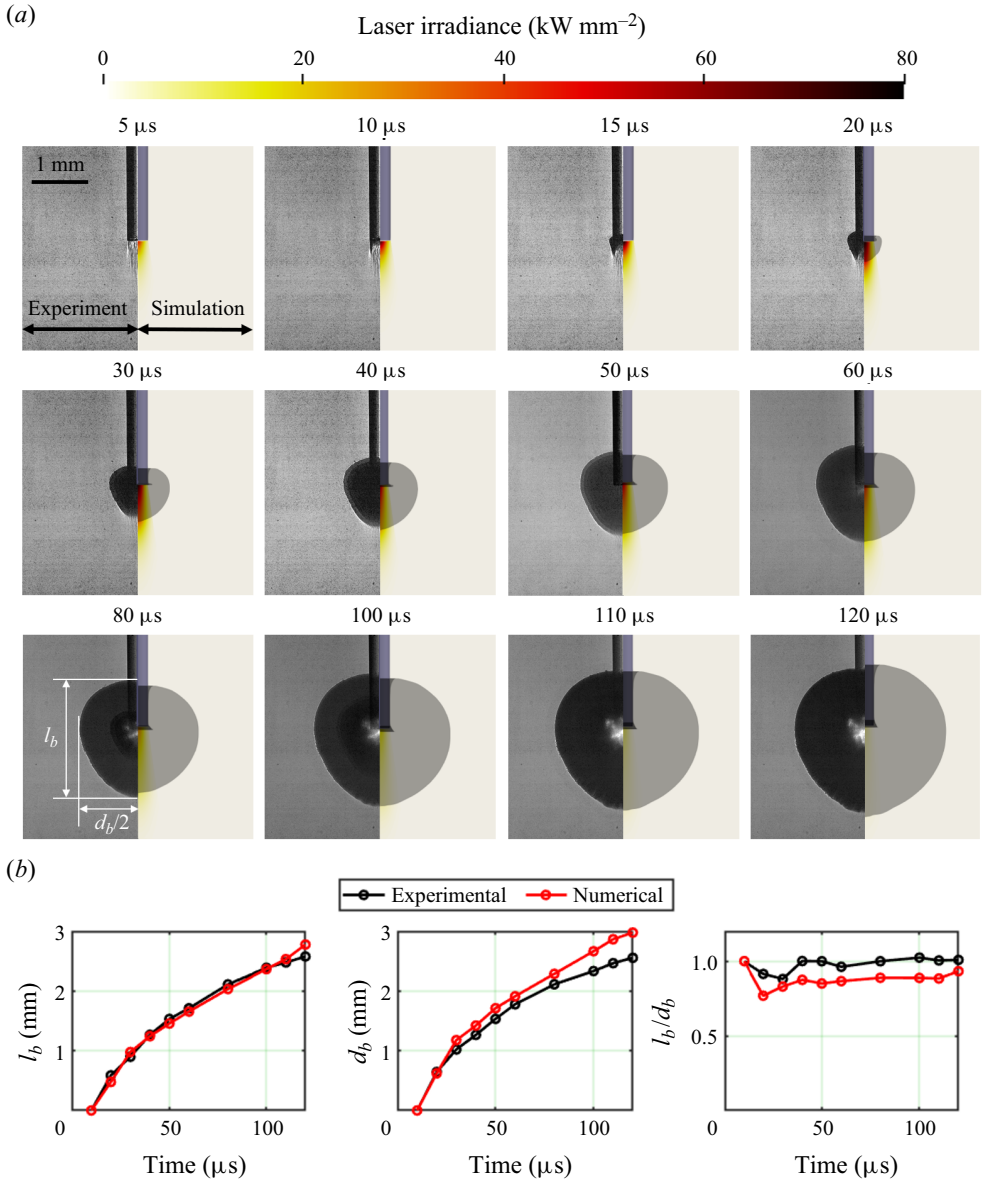

Figure 8. Vapour bubble generated by a Ho:YAG laser: comparison of bubble dynamics obtained from numerical simulation and laboratory experiment. (*a*) Bubble nucleation and evolution. In each subfigure, the left half shows the imaging result from the experiment and the right half shows the bubble and laser irradiance field predicted by the simulation. (*b*) Evolution of bubble size and shape. Here l_b and d_b denote the maximum length of the bubble along and perpendicular to the laser fibre direction, respectively.

simulation result. In figure 8(*a*), the high-speed images obtained from the experiment and the simulation results (bubble dynamics and laser irradiance) are shown side by side. The simulation predicts that the vapour bubble nucleates at approximately 17.4 μs. This is similar to the finding from the experiment, in which the bubble appears at 15 μs. The overall bubble dynamics predicted by the simulation, that is, the evolution of the bubble's size and overall shape, agrees reasonably well with the experimental data.

To make a quantitative comparison between the simulation result and the experimental data, we measure the maximum length of the bubble in two directions, that is, along and perpendicular to the laser fibre direction. These two measurements are denoted as l_b and d_b, respectively, and plotted in figure 8(*b*). The value of l_b obtained from the simulation matches its experiment counterpart very well. The discrepancy between the simulation and the experiment in d_b is a bit larger, between 4 % and 15 % at different time instants. In addition, the bubble's expansion speed in the perpendicular direction is slightly larger in the simulation than in the experiment. Furthermore, the aspect ratio of the bubble, defined as l_b/d_b, is also calculated, and plotted in figure 8(*b*). In both the experiment and the simulation, it varies between 0.75 and 1.

4.2. *Delay of bubble nucleation due to latent heat*

As mentioned in § 4.1.1, the laboratory experiment reveals a delay of bubble nucleation, that is, the time of bubble nucleation is clearly after the time when the vaporisation temperature (T_{vap}) is reached at the fibre tip. The same phenomenon is observed in the simulation.

Figure 9 shows the temperature field at eight time instants during the early period of the simulation. At the beginning, the temperature of water in front of the laser fibre increases continuously, as it absorbs laser energy. This can be seen in the solution snapshots taken at 0 to 7 µs. At 7 µs, the temperature of water next to the centre of the fibre tip first reaches T_{vap}. This is about 10 µs before bubble nucleation, which occurs at 17.4 µs. Within this time period, the region that reaches T_{vap} expands continuously, but phase transition does not occur.

This time delay is due to the fact that water has a high latent heat of vaporisation. Based on the values of l and c_v adopted in the simulation, the latent heat is about 8 times the energy needed to raise water temperature from T_0 to T_{vap}. Using the phase transition model described in § 2.4, as soon as T_{vap} is reached, any additional heat contributes towards increasing the intermolecular potential energy, thereby overcoming the required latent heat of vaporisation. To examine this process more closely, we define

$$\Lambda_\Omega = \int_\Omega \rho \Lambda \, \mathrm{d}\boldsymbol{x}, \tag{4.3}$$

which measures the total amount of latent heat in the computational domain. Figure 10 shows the time history of Λ_Ω. At 6.9 µs, Λ_Ω becomes non-zero and begins to increase. Up to the time of bubble nucleation (17.4 µs), the total energy stored in the latent heat reservoir is around 6.3 mJ. By integrating the power profile (figure 7*d*), we find that this value is approximately 16.84 % of the laser energy input up to the same time.

In this simulation, vaporisation starts at 17.4 µs, and continues for a short period of time (less than 1 µs). Figure 10 shows that after vaporisation stops, Λ_Ω drops to around 0.8 mJ. Given that the total laser pulse energy is 0.2 J, this result implies that only a small fraction of the laser energy input ($(6.3 - 0.8\ \mathrm{mJ})/0.2\ \mathrm{J} = 2.75\ \%$) is directly used to create the bubble.

The enlarged view images in figure 9 reveal that the temperature inside the newly formed vapour bubble is highly non-uniform. In general, this reflects the complexity of the fluid flow inside the bubble, caused by the non-uniform laser beam, the continuation of vaporisation and the laser fibre acting as a wall boundary. Near the bubble's surface, temperature is significantly higher, reaching around 2000 K at 17.4 µs, and displays wavelike perturbations. In contrast, the maximum temperature of the liquid water outside

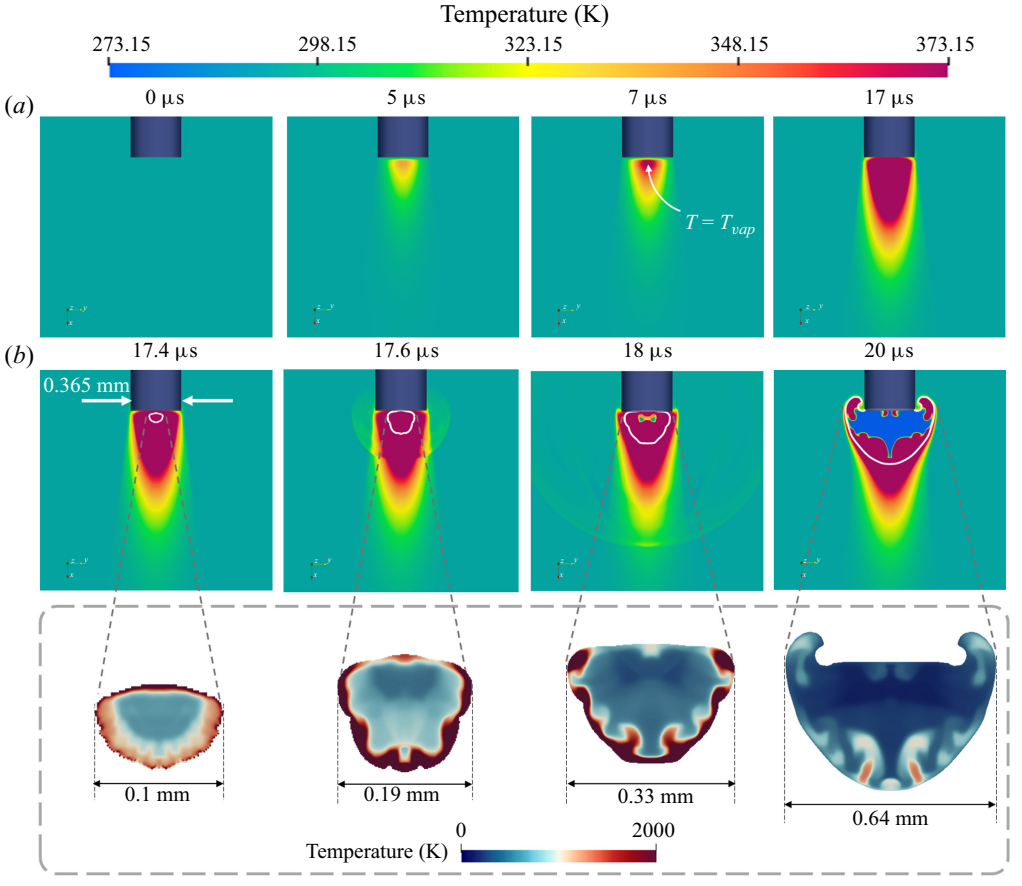

Figure 9. Vapour bubble generated by a Ho:YAG laser: temperature evolution in the first 20 μs. For the solutions between 17.4 and 20 μs, a different colour map is applied to show temperature variation inside the bubble.

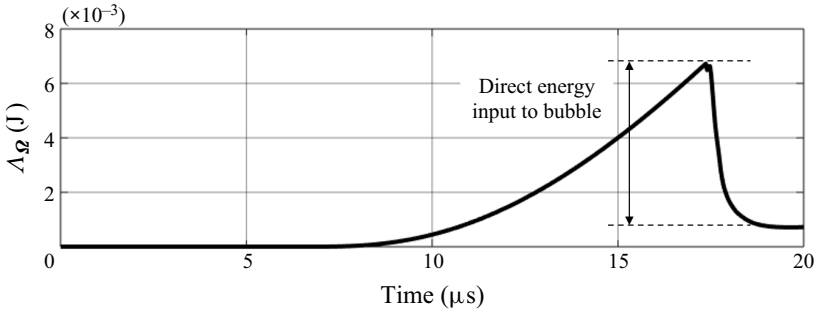

Figure 10. Vapour bubble generated by a Ho:YAG laser: time history of the stored latent heat.

the bubble is 373.15 K (i.e. T_{vap}). Therefore, the temperature field is discontinuous across the bubble's surface, which implies that heat is temporarily trapped inside the bubble. This discontinuity can be explained by the fact that only pressure and normal velocity are enforced to be continuous across the liquid–vapour interface (§ 2.2). Density is not constrained, and is generally discontinuous across the interface. Using the EOSs (2.4)

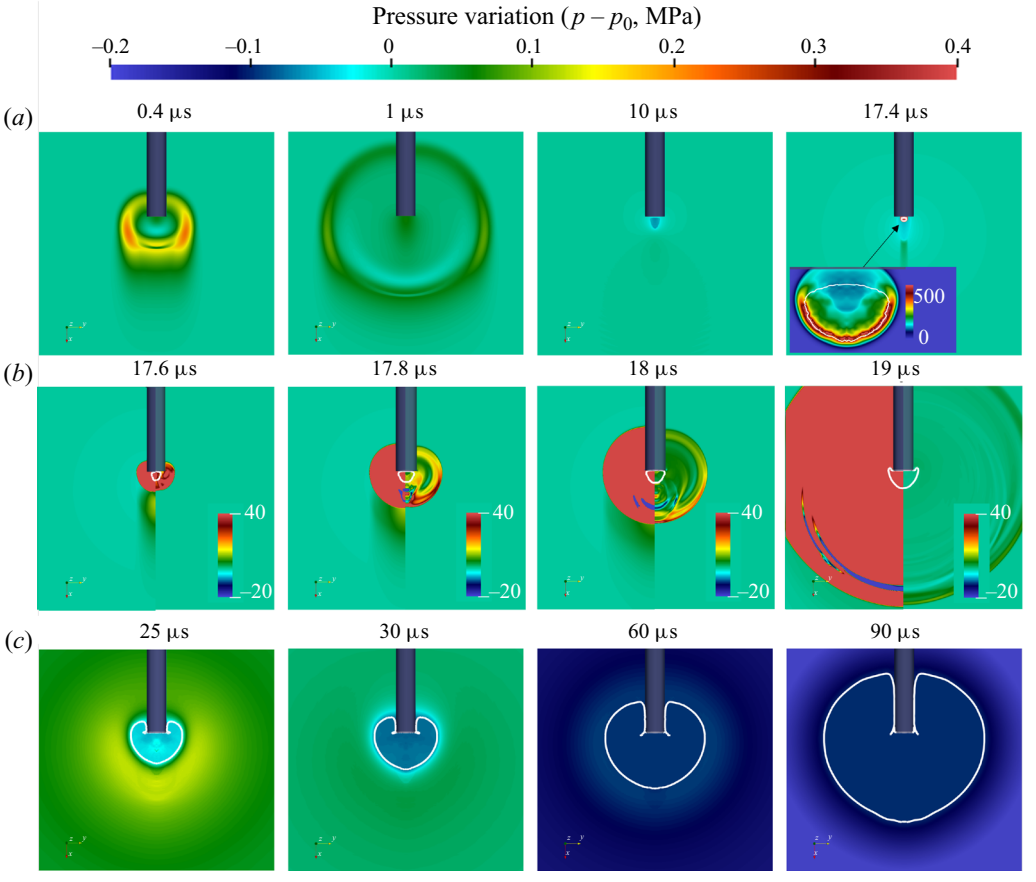

Figure 11. Vapour bubble generated by a Ho:YAG laser: evolution of the pressure field. For the solutions between 17.6 and 19 µs, a different pressure range (−20 to 40 MPa) is applied to clearly show the pressure wave induced by the bubble.

and (2.5), temperature can be written as a function of density and pressure. Due to the discontinuities in both the EOS and density across the interface, the temperature field is also discontinuous. This result may be related to the 'radiation slip' condition in the literature of radiation heat transfer, which is used to account for temperature jumps across material interfaces (Sparrow 2018). It should be noted that although the overall phenomenon of high-temperature perturbation near the bubble's surface can be explained by the physical model, this finding has not been confirmed by experimental measurement. The small size of the initial bubble makes it difficult to completely rule out the influence of numerical discretisation errors. Therefore, details of this phenomenon may not be considered as definitive.

4.3. *Generation of a pear-shaped bubble*

In both the experiment and the simulation, a pear-shaped vapour bubble is obtained. To explain the formation of this shape, we look at the pressure and velocity fields obtained from the simulation (figures 11 and 12).

First, the two pressure snapshots at 0.4 and 1 µs (figure 11) capture an outgoing acoustic wave that emanated from the fibre tip. This is a weak shock wave caused by the rapid

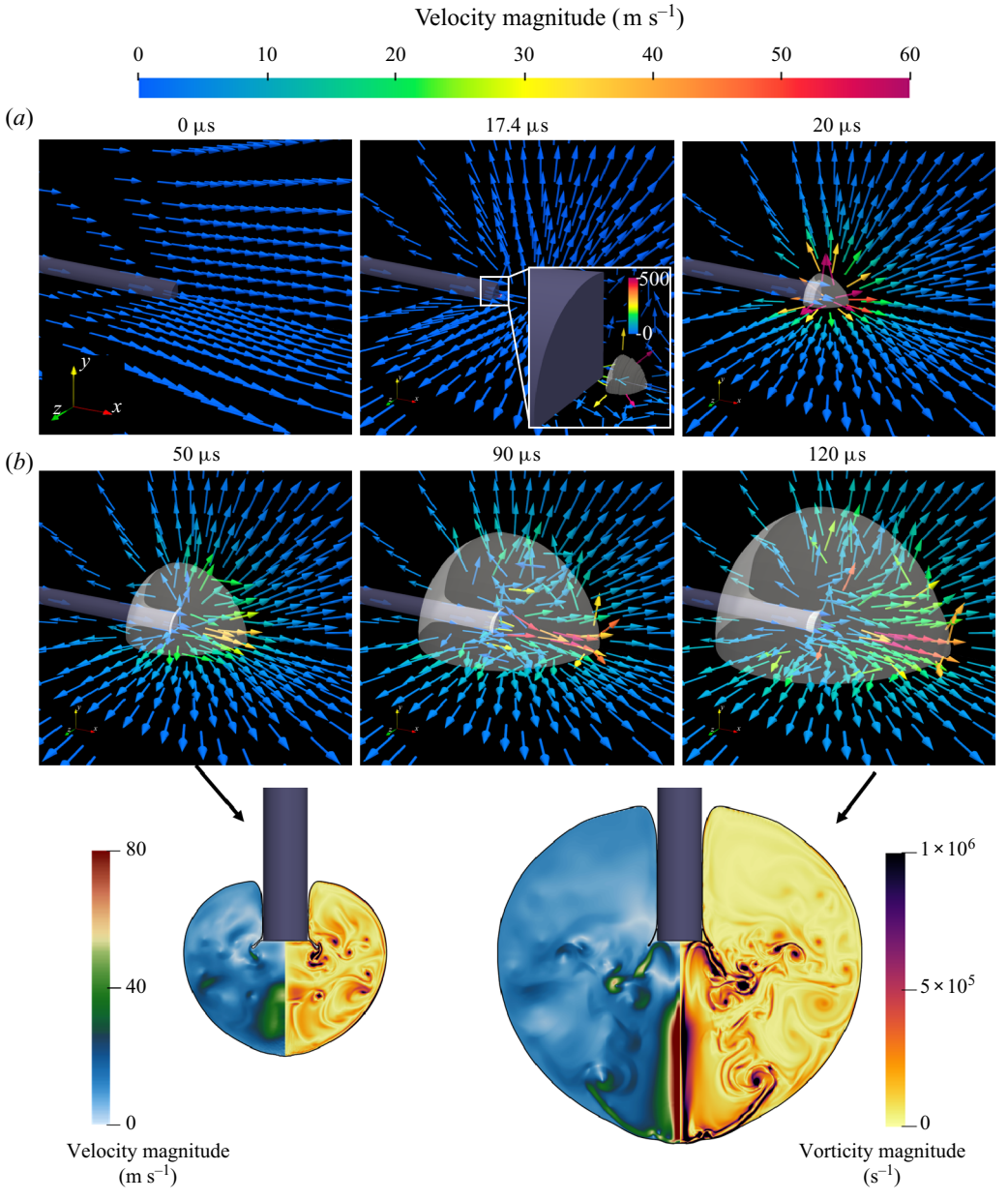

Figure 12. Vapour bubble generated by a Ho:YAG laser: evolution of the velocity field. The solution fields of velocity and vorticity magnitude inside the vapour bubble are shown for the time instants 50 and 120 μs, respectively.

increase of laser power. The vapour bubble nucleates at 17.4 μs. The pressure and velocity fields at this time are shown in figures 11 and 12. At this time, the bubble is already non-spherical. The pressure inside the bubble is high and non-uniform. Specifically, the pressure at the forward end is around 500 MPa. The pressure at the backward end, that is,

near the fibre tip, is much lower, around 100 MPa. This pressure variation is a result of the brief continuation of vaporisation. Regions that have just undergone phase transition have high pressures. Then, the pressure drops as the bubble expands. Therefore, the continuation of vaporisation along the beam direction leads to the higher pressure at the forward end of the bubble. In summary, the simulation result at the time of bubble nucleation (17.4 μs) already implies that the bubble will likely grow into a non-spherical shape, longer in the laser beam direction.

The high pressure inside the initial bubble also generates a weak shock wave that propagates outwards at approximately the speed of sound in water. This wave can be seen in the pressure snapshots taken at 17.6–19 μs (figure 11). This wave is also evident in the temperature snapshots acquired at 17.6 and 18 μs (figure 9). Afterwards, the pressure field becomes quiet, and the bubble continues growing due to inertia. The velocity field at 50–120 μs (figure 12) shows that the velocity around the bubble is non-uniform. It is higher at the forward end of the bubble compared with other regions. Furthermore, the velocity distribution within the bubble exhibits significant non-uniformity. The velocity is notably higher in the vicinity of the central axis of the fibre, particularly near the forward end. This also explains the formation of a pear-like shape, instead of a sphere. In addition, as the bubble expands, small vortices form within the vapour bubble. Two enlarged view images showing these vortices are included in figure 12.

These observations can serve as references to explain the formation of pear-shaped bubbles induced by long-pulsed lasers with similar laser settings. For example, a similar pear-shaped bubble is observed in an experiment detailed in Jansen *et al.* (1996). In this experiment, the bubble is also generated by a Ho:YAG laser with the same pulse energy 0.2 J and a comparable pulse duration 100 μs.

4.4. *Effect of the choice of EOS*

We show that the result obtained from our laser–fluid coupled computational framework can be influenced by the choice of EOS and, more precisely, the choice of EOS parameter values in this case. Here, we present another simulation with a different group of EOS parameter values, listed as Group 2 in table 1. All the other (physical and numerical) parameters remain the same. The results, compared in figure 13, show both parameter groups predict the nucleation of a vapour bubble over a very short period of time, followed by expansion due to high internal pressure, resulting in a rounded bubble shape.

However, a few differences can be found between the two simulations. First, there is a difference in the time when vaporisation occurs. With Group 1 parameter values, vaporisation takes place at 17.4 μs. With Group 2 parameter values, it occurs later, at 18.8 μs. The laser parameters are the same in both cases. Therefore, this discrepancy should be attributed mainly to the different temperature increase rates determined by the EOS, as defined in (2.5). Moreover, the speed of bubble growth is found to be lower with Group 2 parameter values than with Group 1. In figure 13, at both 25 and 30 μs, the bubble obtained with Group 1 parameter values is clearly larger than that obtained with Group 2. The difference in growth speed can be explained by the pressure field. As shown in figure 13(*b*), the bubble's internal pressure reaches a maximum of 73 MPa with Group 2 parameter values. This is much lower than the maximum pressure obtained with Group 1 parameter values, which is 500 MPa. Lastly, the shapes of the bubbles obtained from the two simulations are slightly different. A pear-shaped bubble is captured with Group 1 parameter values. With Group 2, the bubble is more rounded.

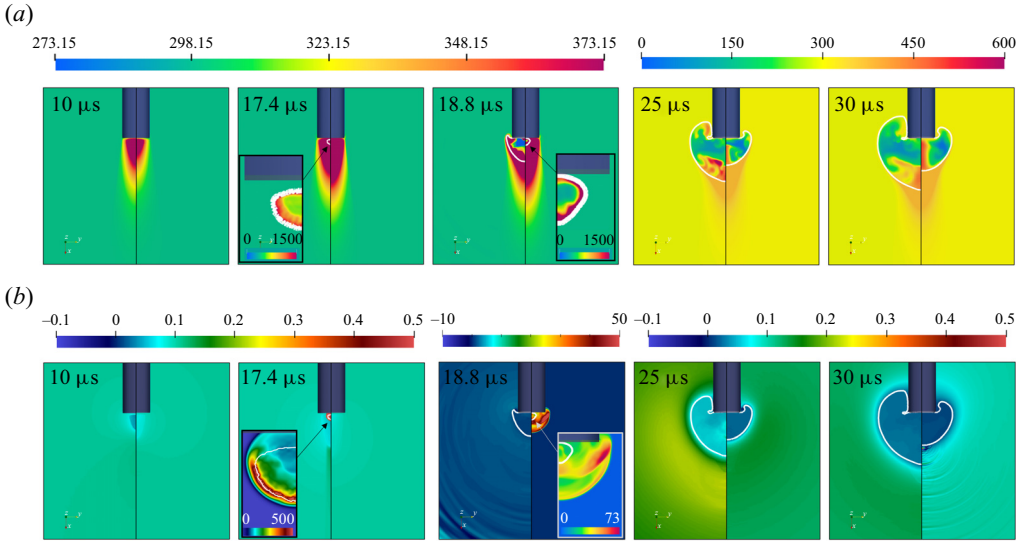

Figure 13. Vapour bubble generated by a Ho:YAG laser: side-by-side comparison of simulation results obtained with different EOS parameter values. In each subfigure, the left and right halves show the result obtained with Group 1 and 2 parameter values, respectively.

5. An elongated bubble

In this section, we investigate the generation of an elongated bubble using Thulium Fibre Laser (TFL). The experiment is conducted in the same acrylic water tank, but the laser wavelength, the beam geometry and the power profile are different. The simulation set-up is modified to match the new experiment. Because of these changes, the vapour bubbles obtained from the experiment and the simulation both have a long, conical shape, different from the pear-shaped bubble shown in § 4. Again, we examine the full-field solutions obtained from the simulation to explain the bubble and fluid dynamics. In addition, we also discuss the effect of bubble dynamics on the delivery of laser energy.

5.1. *Comparison of experimental and numerical results*

5.1.1. *Laboratory experiment*

A TFL (TFL-50/500-QCW-AC, IPG Photonics, Oxford, MA) with a 1940 nm wavelength is used to generate the vapour bubble. The laser generator is operated at the energy level of 0.11 J, which is roughly half of the pulse energy in the Ho:YAG experiment (§ 4.1.1). The diameter of the laser fibre remains the same, but the laser beam is narrower (Blackmon *et al.* 2010). Again, the time history of laser power is measured in air using a photodetector and an oscilloscope (figure 5*b*). The obtained result is shown as the red line in figure 15(*b*). The power profile exhibits a trapezoidal shape, with the laser power fluctuating around 0.6 kW for the first 140 μs. Then, it gradually decays to zero. Compared with the Ho:YAG laser (figure 6*a*), the pulse duration is longer, but the peak power is lower.

Figure 14 shows 12 high-speed images of the vapour bubble during its nucleation and expansion stage (0–120 μs). It can be observed that the laser pulse generates an elongated vapour bubble, clearly different from the pear-shaped bubble obtained with the Ho:YAG laser. Starting from the first frame at $t = 5$ μs, a small bubble appears at the fibre tip. This means vaporisation starts at a time between 0 and 5 μs, earlier than that in the

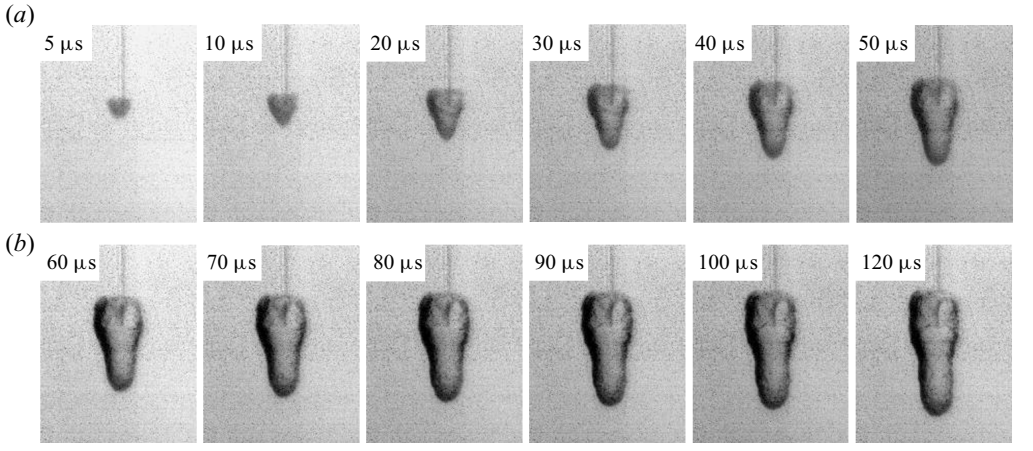

Figure 14. The experimental result obtained with a TFL. (High-speed images of the vapour bubble.)

Ho:YAG experiment. From 5 to 120 μs, the bubble grows continuously, forming a long, conical shape.

5.1.2. *Numerical simulation*

We simulate the TFL experiment using the computational framework described in §§ 2 and 3. The same computational domain and mesh described in § 4.1.2 are adopted. The geometry of the embedded laser fibre is also the same. The divergence angle of the laser beam, θ_{div}, is set to 9.78°. This is because the wavelength of TFL is different from that of the Ho:YAG laser. The absorption coefficient, μ_α, is set to 14 mm^{-1} in liquid water (Traxer & Keller 2020), which is about 6 times the value for Ho:YAG laser. This is also due to the fact that TFL has a different wavelength. The absorption coefficient in water vapour is set to 0.001 mm^{-1}, the same as in the previous case.

The waist radius of the Gaussian beam is set to 0.05 mm (figure 15*a*). This value is also determined through calibration, considering that TFL typically exhibits greater collimation, which results in a smaller beam waist compared with the Ho:YAG laser (Fried 2018). The temporal profile of the laser power is specified to be a trapezoidal function that approximates the experimental measurement (figure 15*b*). The resulting pulse energy is the same as that in the experiment, i.e. 0.11 J. More specifically, the power grows rapidly from 0 to 0.62 kW within 0.1 μs. This peak power is maintained for a period of 140 μs. Then, it vanishes gradually within 80 μs. The parameters of the Noble–Abel stiffened gas EOS are set by the values in Group 1 in table 1.

The simulation predicts the formation of an elongated bubble, similar to that observed in the experiment. Figure 16(*a*) presents a side-by-side comparison between the results obtained from the experiment and the simulation. In each subfigure, the left-hand side is a high-speed image obtained from the experiment. The right-hand side is the simulation result at the same time, showing the bubble surface and the laser irradiance field. It can be seen that the bubble obtained from the simulation also has a long, conical shape. In the simulation, vaporisation starts at 1.2 μs. This is consistent with the experimental data, which shows the bubble nucleates at a time between 0 and 5 μs. At 5 μs, the shape of the bubble obtained from the simulation matches the experimental data reasonably well. As time progresses, the bubble from the simulation undertakes the same evolution trend, growing faster in the axial direction than in the radial direction. The main difference

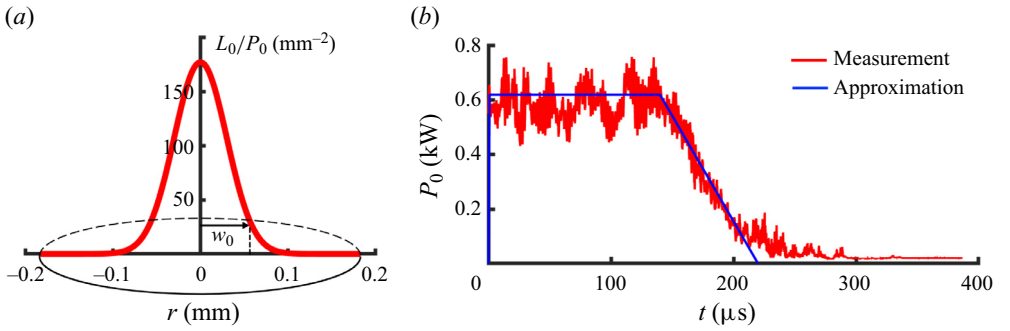

Figure 15. Vapour bubble generated by a TFL: simulation set-up. (*a*) Spatial profile of laser irradiance on the source plane. (*b*) Temporal profile of laser power.

between the simulation result and the experimental data lies in the size of the bubble. The simulated bubble is smaller than its experimental counterpart in all the snapshots shown in figure 16(*a*).

To make a quantitative comparison, we measure the length and width of the bubble, denoted by l_b and d_b, respectively. Figure 16(*b*) shows the time histories of l_b, d_b, and the aspect ratio, l_b/d_b. It can be observed that the aspect ratio predicted by the simulation matches well the experimental result. For l_b and d_b, the simulation is able to capture the same trend found in the experiment. But the magnitude is lower. It is notable that in both the simulation and the experiment, the aspect ratio starts at approximately 1. Then, it increases steadily, reaching around 2 after 70 μs. This implies that the bubble elongates gradually. In comparison, in the previous case with the Ho:YAG laser, the l_b-to-d_b aspect ratio is roughly constant in time (figure 8*b*).

5.2. *Bubble elongation due to continuous vaporisation*

To investigate the mechanism of bubble elongation, we examine the temperature, pressure and velocity fields obtained from the simulation.

Figure 17 presents the evolution of the temperature field near the fibre tip in the first 5 μs. The laser irradiance field is also shown at three time instants (1.2, 2.0 and 2.4 μs) to facilitate the discussion. Similar to the previous case (figure 9), water temperature increases due to the absorption of laser energy, especially in the region around the central axis of the laser beam. The time it takes to reach the vaporisation temperature is significantly shorter, only 0.4 μs, compared with 7 μs in the previous case. The faster temperature increase can be attributed to two factors. First, the smaller beam waist of the laser results in a more concentrated distribution of laser irradiance on the source plane. Although the laser power is lower in the current case (compare figures 8(*d*) and 16(*b*)), the more concentrated distribution leads to a higher laser irradiance along the central axis, that is, 110 kW mm^{-2} (figure 16*a*) vs 80 kW mm^{-2} in the previous case (figure 8*a*). Second, the absorption coefficient of TFL in water is significantly higher than that of the Ho:YAG laser used previously (14 vs 2.42 mm^{-1}). The time delay in bubble nucleation is also observed in this case. After T_{vap} is reached, it takes another 0.8 μs before vaporisation occurs at the fibre tip, at 1.2 μs. Within this time period, the absorbed laser energy is converted into the intermolecular potential energy of liquid water.

A major difference from the previous case is that with the TFL, vaporisation continues for a much longer period of time, that is, from 1.2 until 53.5 μs. In addition, it happens

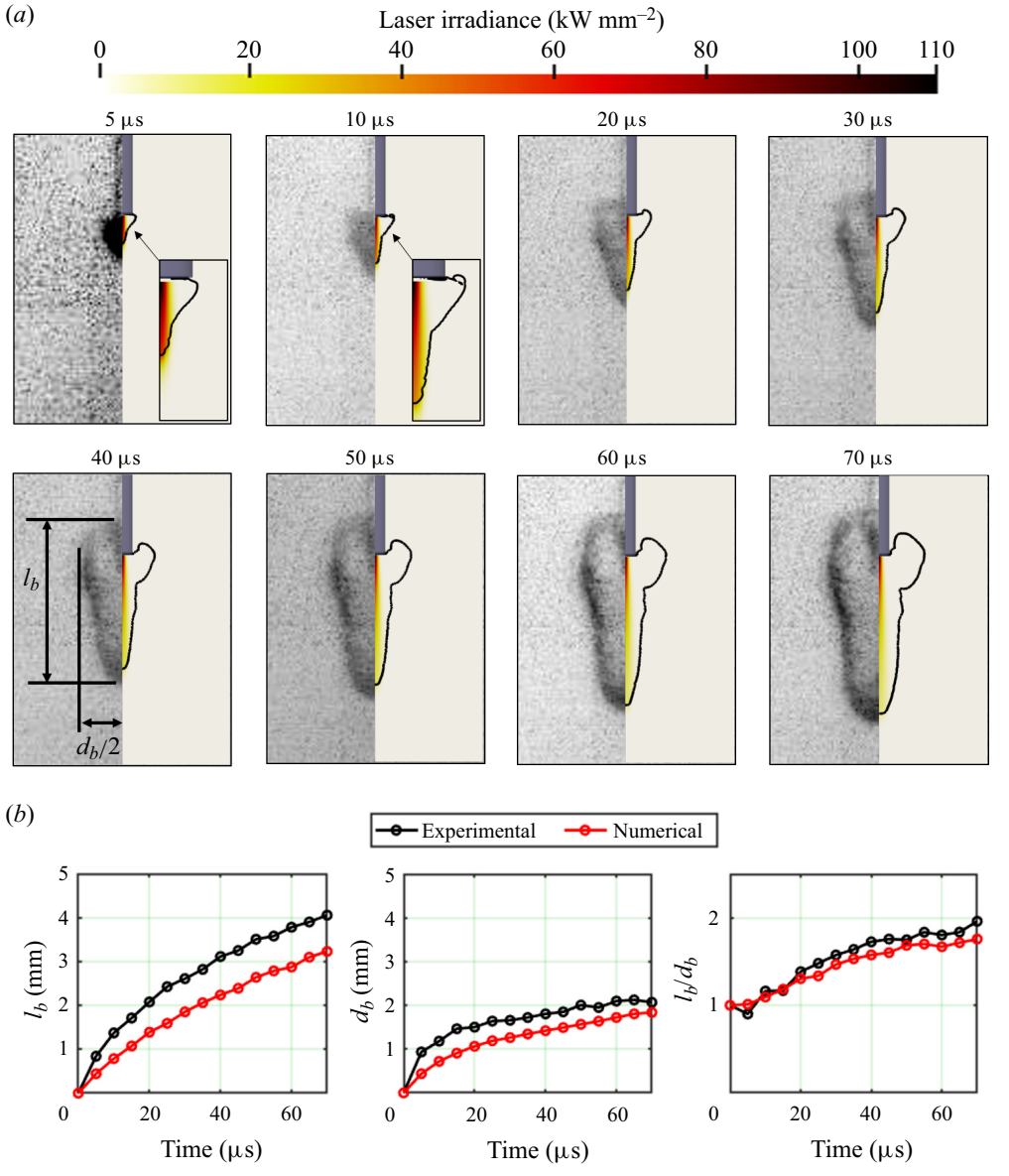

Figure 16. Vapour bubble generated by a TFL: comparison of bubble dynamics obtained from numerical simulation and laboratory experiment. (*a*) Bubble nucleation and evolution. In each subfigure, the left-hand side shows the imaging result from the experiment and the right-hand side shows the bubble and laser irradiance field predicted by the simulation. (*b*) Evolution of bubble size and shape. Here l_b and d_b denote the maximum length of the bubble along and perpendicular to the laser fibre direction, respectively.

mainly along the central axis of the laser beam, which drives the bubble to grow in the same direction.

Initially, a small, rounded bubble emerges in front of the laser fibre. This is shown in figure 17, in the snapshot taken at 1.2 μs. Because the vapour phase does not absorb laser energy (μ_α set to 0.001 mm^{-1}), the small bubble extends the laser beam along the axial direction. This effect can be seen in the inset images in figure 17. As a result,

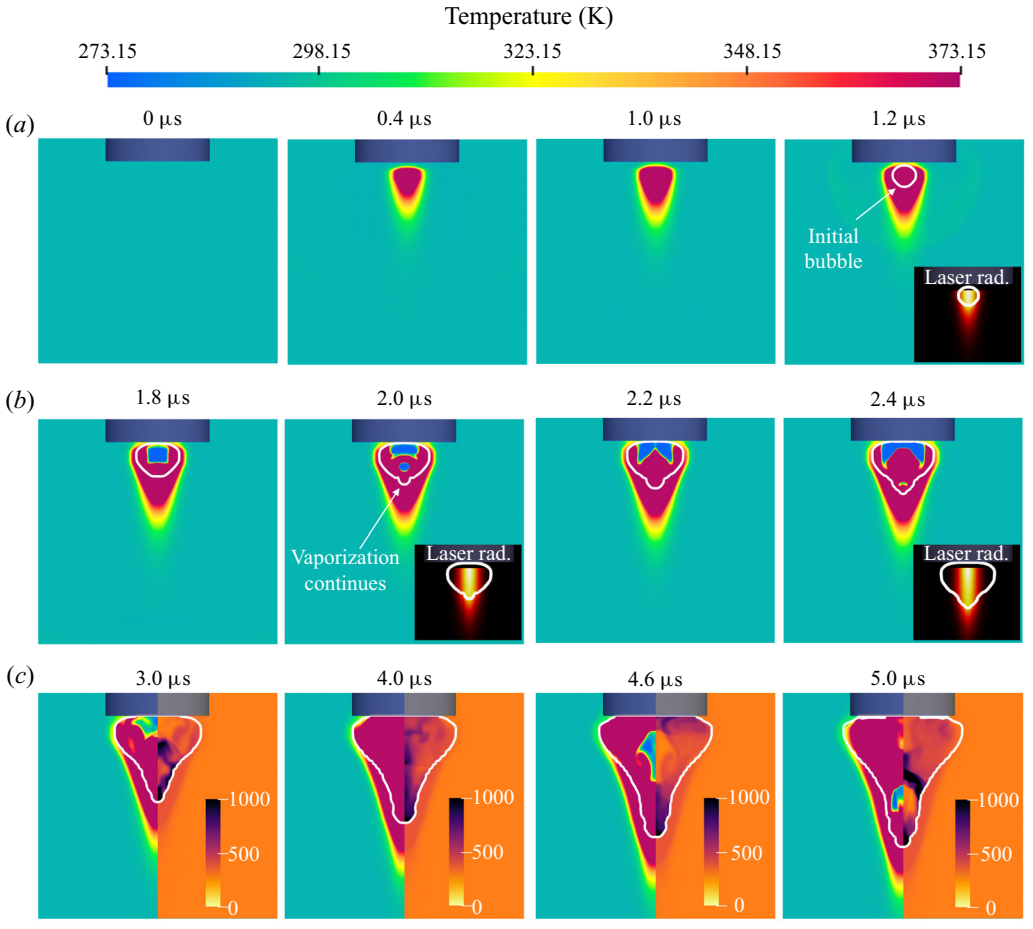

Figure 17. Vapour bubble generated by a TFL: evolution of the temperature field in the first 5 μs. For the solutions between 3.0 and 5.0 μs, a different colour scheme and range is applied to clearly show the temperature variation inside the bubble. The solution of laser irradiance is shown at 1.2, 2.0 and 2.4 μs (colour range 0–110 kW mm^{-2}) as a reference.

the liquid water next to the bubble's forward end, that is, the forward-most point along the axial direction, experiences a sudden increase in laser irradiance, which accelerates the accumulation of energy there to overcome the latent heat of vaporisation. From the simulation result, we observe the continuation of phase transition in this direction. For example, the snapshot taken at 2.0 μs captures a bulge at the bubble's forward end, which is a newly vaporised region. At the same time, the high pressure inside the bubble also drives it to expand in both axial and radial directions. The combination of these two processes, that is, phase transition and advection, drives the bubble to grow into a long, conical shape.

Figure 18 presents the evolution of the pressure field up to 70 μs. At the beginning, the sudden increase of temperature due to the absorption of laser leads to a weak shock wave at the fibre tip. The snapshot taken at 1 μs captures this phenomenon, where the maximum pressure is found to be less than 0.5 MPa. Next, the snapshot taken at 1.2 μs captures the pressure field inside and around the initial bubble. The peak pressure inside the bubble is found to be 94 MPa at this time. This high pressure drives the bubble to

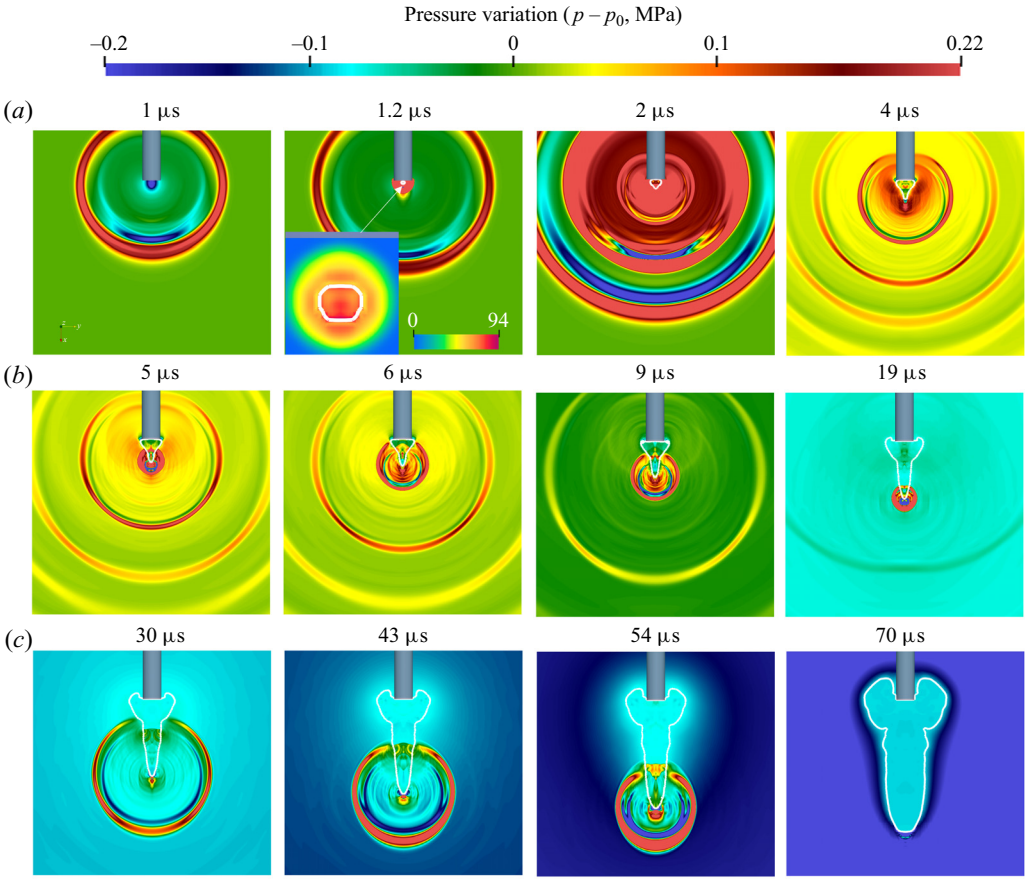

Figure 18. Vapour bubble generated by a TFL: evolution of the pressure field.

expand in all directions. It also generates a weak shock wave that propagates outwards, at approximately the speed of sound in liquid water. Because of the small size of the initial bubble, the pressure magnitude of this wave quickly decays to less than 1 MPa. Compared with the pressure field obtained from the Ho:YAG laser (figure 11), the main difference here is that as phase transition continues, acoustic waves keep emanating from the bubble's forward tip. This phenomenon is captured by all the snapshots taken between 2 and 50 μs. In the current simulation, phase transition stops at 53.5 μs. Afterwards, the pressure field becomes quiet. As shown in the snapshot at 70 μs, the main feature is that the bubble's internal pressure is higher than the ambient value. Therefore, the bubble continues growing. By this time, it has already formed a long, conical shape.

Figure 19 shows the evolution of the velocity field. The inset image at 1.2 μs shows that when the initial bubble has just formed, the high internal pressure leads to high velocity in both axial and radial directions. This phenomenon is also found in the previous case (figure 12, 17.4 μs). In the previous case, the bubble's velocity quickly starts to decrease. In the current case, however, the velocity inside the bubble remains high. This is again because of the continuation of phase transition, as it keeps adding energy to the existing bubble. In addition, multiple vortexes are observed inside the vapour bubble as shown in the snapshots at 70 μs, which is related to the propagation of multiple acoustic waves

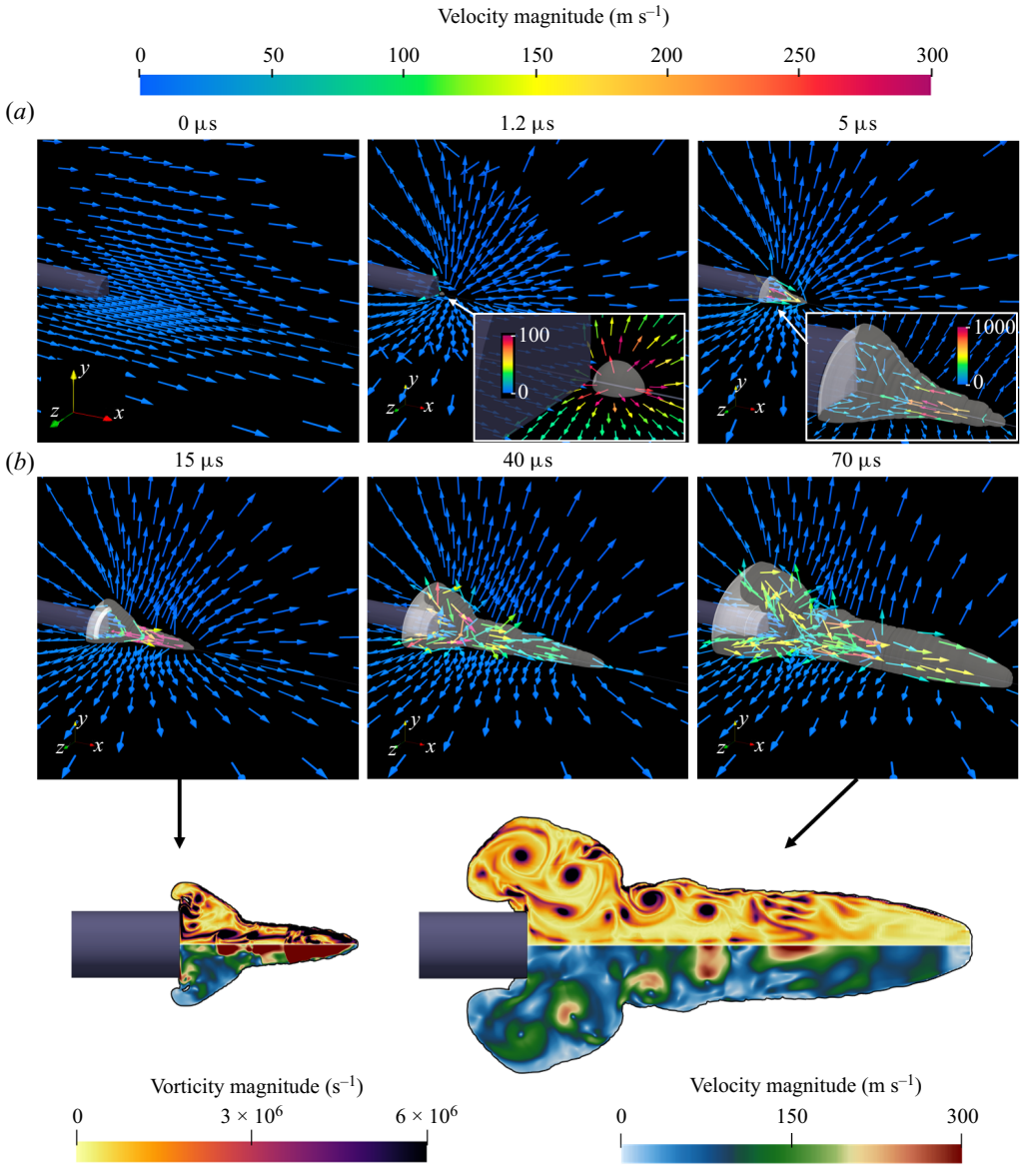

Figure 19. Vapour bubble generated by a TFL: evolution of the velocity field. The solution fields of velocity and vorticity magnitude inside the vapour bubble are shown for the time instants 15 and 70 μs, respectively.

emitted from the bubble's forward tip. Therefore, the evolution of the velocity field also suggests that phase transition plays a substantial role in the bubble's dynamics.

5.3. *Moses effect*

Compared with liquid water, the absorption of laser by water vapour is negligible. Therefore, the formation of a vapour bubble along the path of the laser beam allows laser energy to be transmitted over a longer distance. This phenomenon, shown in figure 17, is sometimes referred to as the Moses effect, after the story of Moses parting

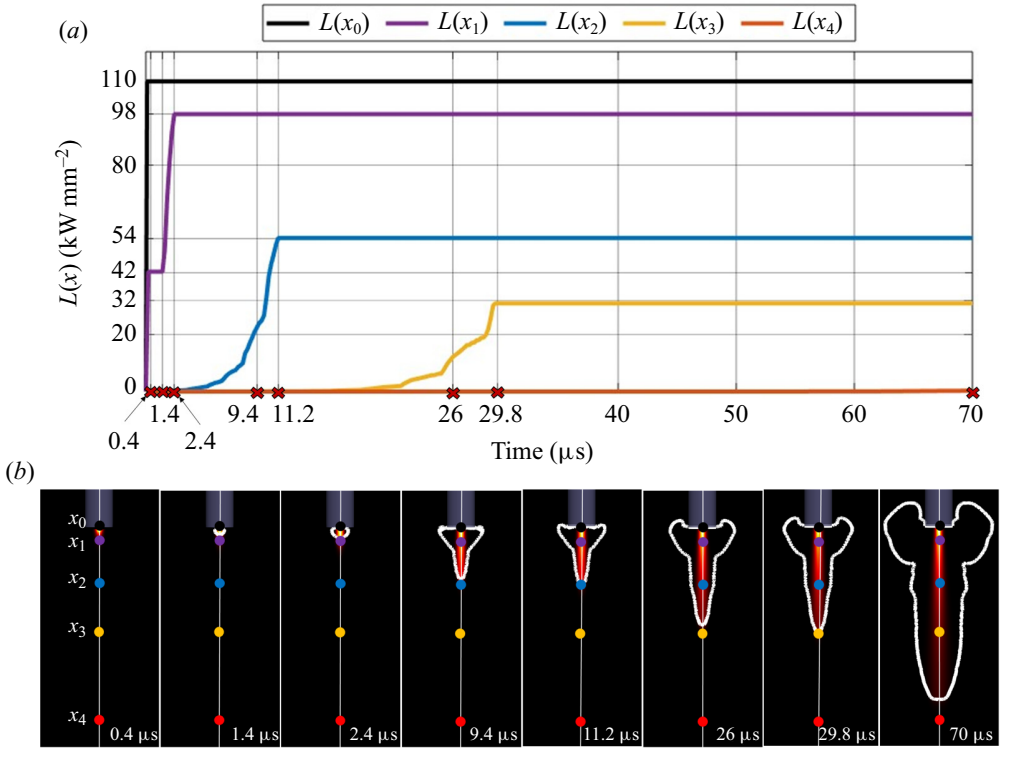

Figure 20. Vapour bubble generated by a TFL: Moses effect.

the sea (van Leeuwen *et al.* 1993; Ventimiglia & Traxer 2019). To investigate this effect more closely, we introduce four sensor points along the central axis of the laser beam, at difference distances from the fibre tip. Their coordinates (in millimetres) are $\boldsymbol{x}_1 : (-0.3, 0, 0)$, $\boldsymbol{x}_2 : (0.3, 0, 0)$, $\boldsymbol{x}_3 : (1.1, 0, 0)$ and $\boldsymbol{x}_4 : (2.7, 0, 0)$. The fibre tip is at $\boldsymbol{x}_0 : (-0.5, 0, 0)$, as shown in figure 7(*b*). Figure 20 shows the time history of laser irradiance at the four sensor locations, as well as the fibre tip.

Before bubble nucleation (1.2 μs), most of the laser energy is absorbed by a small volume of water next to the fibre tip. Although Sensor 1 is only 0.2 mm from the fibre tip, the laser irradiance at this point has already dropped to 37.6 % of the value at the fibre tip. The laser irradiance at the other sensor locations is negligible. This means without the vapour bubble, the laser cannot reach Sensors 2, 3 and 4.

After bubble nucleation, the laser irradiance at all the sensor points starts to increase. At 2.4 μs, the bubble reaches $\boldsymbol{x}_1$. At this time, the laser irradiance at Sensor 1 reaches the maximum value, 98 kW mm^{-2}. It is still lower than the laser irradiance at the fibre tip, but this is only because the laser beam has a 9.78° divergence angle.

The time histories of laser irradiance at Sensors 2 and 3 follow the same trend. As the vapour bubble's forward end gets close to the sensor, laser irradiance increases. The maximum value is reached when the bubble reaches the sensor. The maximum laser irradiance decreases along the axial direction, due to beam divergence. Sensor 4 is placed at 3.2 mm from the fibre tip. At 70 μs, the bubble's forward tip is still more than 0.29 mm from it. As the result, the laser irradiance at Sensor 4 remains nearly zero.

In summary, the simulation result shows that the vapour bubble essentially creates a channel that allows laser to pass through. Compared to rounded bubbles, the long, conical shape obtained in the current case (both the experiment and the simulation) can be advantageous as it provides a longer channel.

6. Transition between pear-shaped and elongated bubbles

6.1. *A race between advection and phase transition*

Using different laser settings, we have obtained two vapour bubbles in different shapes, namely a rounded, pear-like shape shown in § 4 and a long, conical shape shown in § 5. Depending on the application, one or the other may be preferred. By examining the simulation result, we find that a major difference between the two cases is that in the first case, vaporisation only lasts for a short period of time, less than 1 μs. In the second case, vaporisation continues along the laser beam direction for over 50 μs. It is also clear that in both cases, a newly vaporised region carries a high pressure (from the accumulated latent heat) that drives the existing bubble to expand by means of advection. Therefore, the simulation result suggests that when laser energy input is maintained in time (i.e. long-pulsed laser), the vapour bubble's shape is influenced by two factors:

(1) the speed of bubble growth by advection; and
(2) the speed of bubble growth by phase transition.

Furthermore, the simulation result indicates that the transition between pear-shaped and elongated bubbles may be related to a competition between these two speeds. At least one of the two speeds must have changed from one case to the other. In other words, at least one of them is controllable.

Unfortunately, the fluid dynamics is highly nonlinear and multi-dimensional. It is impossible to separate the two speeds from the governing equations. In order to define and examine the two speeds analytically, we resort to a simplified model problem.

As illustrated in figure 21(*a*), we consider an initial vapour bubble of spherical shape, with radius R_0. We assume it has an internal pressure p_{Go} that is higher than the ambient pressure p_∞, which drives the bubble to expand. For this problem, the bubble dynamics can be modelled by the Rayleigh–Plesset equation (Brennen 2014). After dropping the viscosity and surface tension terms for simplicity, we get

$$R\frac{\mathrm{d}^2R}{\mathrm{d}t^2}+\frac{3}{2}\left(\frac{\mathrm{d}R}{\mathrm{d}t}\right)^2=\frac{p_{Go}}{\rho_0}\left[\left(\frac{R_0}{R}\right)^{3\gamma}-\frac{p_\infty}{p_{Go}}\right], \tag{6.1}$$

where ρ_0 denotes the density of the liquid phase and γ denotes the specific heat ratio of the vapour phase. In this case, the bubble's dynamics is isotropic, and driven only by advection. Therefore, we define the speed of bubble growth by advection as

$$v_{adv}(t)=\frac{\mathrm{d}R(t)}{\mathrm{d}t}, \tag{6.2}$$

where $R(t)$ is the solution of (6.1).

From (6.1), it is clear that v_{adv} depends on p_{Go} and R_0. If the initial bubble is created through vaporisation, p_{Go} is determined by the thermodynamics of water, including its latent heat of vaporisation (§ 2.4). Therefore, it may not always be adjustable. To see the

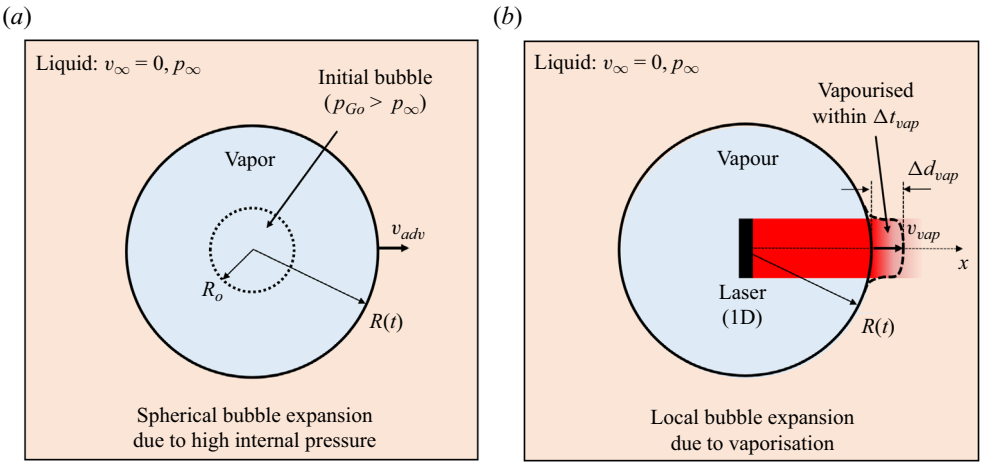

Figure 21. Illustration of a simplified model problem for which the speeds of advection (v_{adv}) and phase transition (v_{vap}) are defined.

effect of R_0, we first note that if we rewrite (6.1) with

$$\tau = \frac{t}{R_0} \quad \text{and} \quad \hat{R}(\tau) = \frac{R}{R_0}, \tag{6.3a,b}$$

R_0 can be eliminated from the equation. Specifically, we have

$$\hat{R}\frac{\mathrm{d}^2\hat{R}}{\mathrm{d}\tau^2} + \frac{3}{2}\left(\frac{\mathrm{d}\hat{R}}{\mathrm{d}\tau}\right)^2 = \frac{p_{Go}}{\rho_L}\left[\left(\frac{1}{\hat{R}}\right)^{3\gamma} - \frac{p_\infty}{p_{Go}}\right], \tag{6.4}$$

and the solution $\hat{R}(\tau)$ is independent of R_0. In addition, substituting (6.3*a*,*b*) into (6.2) yields

$$v_{adv} = \frac{\mathrm{d}R(t)}{\mathrm{d}t} = \frac{\mathrm{d}\hat{R}(\tau)}{\mathrm{d}\tau}. \tag{6.5}$$

Therefore, changing the value of R_0 leads to a linear scaling (i.e. stretching or compressing) of v_{adv} in time, while the peak values remain the same. If the initial bubble is created by vaporisation, R_0 may be controlled by adjusting the spatial distribution of the heat source. For example, a more uniform distribution of the laser power on the source plane may lead to a larger R_0.

Next, we assume that at a time $t > 0$, a uniform, parallel laser beam is activated, and it creates a bulge on the bubble surface through vaporisation (figure 21*b*). We assume that over a short period of time, the vaporised region (i.e. the bulge) has a cylindrical shape, with a depth of Δd_{vap}. To model the continuation of vaporisation, we assume that at time t, $T = T_{vap}$ within this cylindrical region, and $\Lambda = l$ at $x = R(t)$. This assumption is justified by the results of the simulations shown in §§ 4 and 5.

The energy required to vaporise the forward end of the cylindrical region, i.e. $x = R(t) + \Delta d_{vap}$, can be estimated by

$$\Delta E = \rho_0[l - \Lambda(R(t) + \Delta d_{vap}, t)], \tag{6.6}$$

where ρ_0 denotes the density of the liquid phase, assumed to be a constant. The time to obtain this amount of energy from the laser beam can be estimated by

$$\Delta t_{vap} = \frac{\Delta E}{\mu_\alpha L(R(t) + \Delta d_{vap}, t)} = \rho_0 \frac{l - \Lambda(R(t) + \Delta d_{vap}, t)}{\mu_\alpha L(R(t) + \Delta d_{vap}, t)}. \tag{6.7}$$

Now, we define the speed of bubble growth by phase transition as

$$v_{vap} = \lim_{\Delta d_{vap} \to 0^+} \frac{\Delta d_{vap}}{\Delta t_{vap}}. \tag{6.8}$$

Substituting (6.7) into (6.8), and noting that $\Lambda(R(t), t) = l$, we get

$$v_{vap}(t) = -\frac{\mu_\alpha L(R, t)}{\rho_0 \left.\dfrac{\partial \Lambda}{\partial x}\right|_{x=R(t)}}. \tag{6.9}$$

The derivative $\partial \Lambda / \partial x$ is negative, as the laser energy input decreases along the beam direction. Therefore, v_{vap} is positive. It is notable that the latent heat of vaporisation, l, is not involved in (6.9). Intuitively, the latent heat represents an energy threshold for phase transition to occur. Once this threshold is reached, it may not influence the speed of bubble growth by phase transition. Equation (6.9) also indicates that v_{vap} may be controlled by adjusting the laser's wavelength and power, which will lead to variations in μ_α and L.

6.2. *Testing hypothesis using simulation results*

We hypothesise that a race between advection and phase transition determines the morphing of the vapour bubble. In the previous subsection, we have defined speeds v_{adv} and v_{vap} for a simplified model problem. In real-world applications, these quantities would have to be estimated using available data. We hypothesise that at any time, if v_{adv} is greater than v_{vap}, the bubble tends to grow spherically. If v_{adv} is smaller than v_{vap}, the bubble tends to elongate along the laser beam direction.

This hypothesis can be tested using our simulation results. Figure 22 illustrates the method adopted here to estimate v_{adv} and v_{vap}. Although this figure only shows a solution snapshot obtained from the TFL simulation, the same estimation method is also applied to the other simulation with a Ho:YAG laser.

Because vaporisation mainly continues along the laser beam direction, we estimate the advection speed, v_{adv}, by measuring the speed of bubble expansion in the radial direction, outside the beam waist. Specifically, we define a small time interval, $\Delta t_{adv} = 0.2$ µs. The radial expansion of the bubble over this time interval, Δd_{adv} (figure 22), is measured at 255 time points for the Ho:YAG simulation and 320 time points for the TFL simulation. At each time point, v_{adv} is estimated by

$$\bar{v}_{adv} = \frac{\Delta d_{adv}}{\Delta t_{adv}}. \tag{6.10}$$

To estimate the phase transition speed, v_{vap}, we look at the forward tip of the bubble, denoted by $x_{max}(t)$ in figure 22. We specify a small distance, $\Delta d_{vap} = 0.0015$ mm, along the laser beam direction. Then, we extract the simulation result of L and Λ to evaluate (6.7), which gives us Δt_{vap}, that is, an estimate of the time needed to extend the bubble

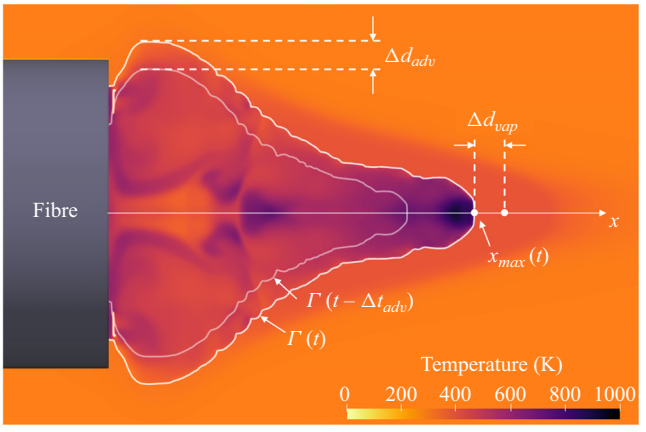

Figure 22. Illustration of the method to estimate v_{adv} and v_{vap} using simulation results. The actual sizes of Δd_{adv} and Δd_{vap} used in the estimation are smaller than those shown in the figure. The temperature field is obtained from the simulation presented in § 5, at $t = 4.8$ µs.

front by Δd_{vap}. Then, we estimate v_{vap} by

$$\bar{v}_{vap} = \frac{\Delta d_{vap}}{\Delta t_{vap}}, \tag{6.11}$$

which is consistent with its definition in (6.8). Again, we calculate $\bar{v}_{vap}$ at 255 time points for the Ho:YAG simulation and 320 time points for the TFL simulation.

Figure 23 shows the time histories of $\bar{v}_{adv}$ and $\bar{v}_{vap}$ obtained from the two simulations. For the Ho:YAG simulation that generated a pear-shaped bubble, $\bar{v}_{adv}$ is found to be roughly two orders of magnitude higher than $\bar{v}_{vap}$ over the entire time period shown in the figure. This is consistent with the finding that in this case, bubble expansion is mainly driven by advection, whereas phase transition only lasts for less than 1 µs. It also supports our hypothesis that if v_{adv} is greater than v_{vap}, the bubble tends to grow spherically. For the TFL simulation that generated an elongated bubble, $\bar{v}_{vap}$ is found to be higher than $\bar{v}_{adv}$. Their difference is more than one order of magnitude in the early period of the simulation. But after 20 µs, the difference starts to become smaller. This is consistent with the finding that in this case, phase transition continues for a long period of time, until 53.5 µs. It also supports our hypothesis that if v_{adv} is smaller than v_{vap}, the bubble tends to elongate along the laser beam direction.

In summary, the simulation results suggest that the transition between pear-shaped and elongated bubbles is determined by a race between advection and phase transition. These two speeds can be characterised by v_{adv} and v_{vap}, which are mathematically defined for a simplified model problem. Here v_{adv} and v_{vap} depend on the laser setting and the properties of the fluid medium. This conclusion can be used as a reference to explain the observations in the earlier experiments conducted by other researchers. For example, the study by Asshauer *et al.* (1994) shows that applying a higher laser source irradiance (1150 vs 86 kW cm^{-2}) results in the generation of an elongated bubble instead of a pear-shaped one. This observation aligns with our conclusion, where the higher laser source irradiance leads to an increased vaporisation velocity. In addition, in real-world applications, it may be possible to obtain a preferred bubble shape by adjusting the relevant parameters based on this conclusion. For example, in our TFL experiment, the laser absorption coefficient and the source laser irradiance are both higher than their counterparts in the

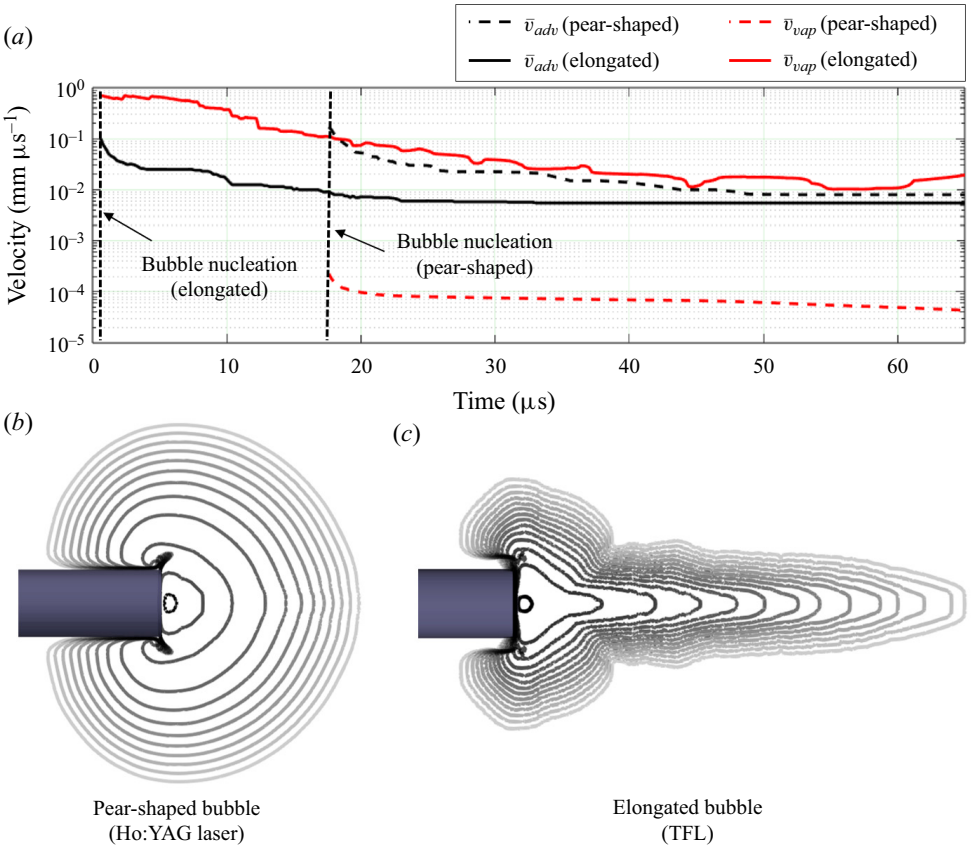

Figure 23. Estimation of v_{adv} and v_{vap} for the pear-shaped bubble obtained with Ho:YAG laser (§ 4) and the elongated bubbles obtained with TFL (§ 5). The bubble dynamics is also shown by superimposing simulation results at different time instants.

Ho:YAG experiment. These changes lead to a significant increase of v_{vap} by about 2 orders of magnitude. In comparison, the variation of v_{adv} is much smaller. Therefore, the changes in laser setting make v_{vap} higher than v_{adv}. As a result, an elongated bubble is obtained.

7. Concluding remarks

In this work, we have applied a laser–fluid computational model to study the physics behind vapour bubbles generated by long-pulsed lasers. The long pulse duration essentially means that three different physical processes, laser radiation, phase transition (i.e. vaporisation) and fluid dynamics, overlap both in time and in space. Their interaction adds complexity to the problem, but also makes it more interesting. Unlike short-pulsed lasers that usually produce spherical bubbles (assuming no influence from material boundaries), long-pulsed lasers can generate both rounded and elongated bubbles when operated in different settings.

In two separate laboratory experiments, we used a Ho:YAG laser and TFL to generate a rounded pear-shaped bubble and an elongated conical bubble. In each case, the laser power profile is also measured, and used as an input to the simulation. The computational model combines laser absorption, vaporisation and the dynamics and thermodynamics of

a compressible two-phase fluid flow. The two simulations for a Ho:YAG laser and THL are performed with the same fluid parameters, such as the EOS parameters, the latent heat of vaporisation and thermal diffusivity. In both cases, the predicted bubble shape evolution matches the experimental data reasonably well. The simulation results show that the three physical processes mentioned previously interact in multiple ways, including the following.

(1) The activation of laser radiation may create a weak shock wave in the fluid flow.
(2) The absorption of laser increases the thermal energy and intermolecular potential energy of liquid water, eventually leading to its vaporisation.
(3) The nucleation of a vapour bubble creates a new material subdomain (i.e. vapour) in which laser can transmit almost losslessly.
(4) Because water has a high latent heat of vaporisation, the bubble initially has a high internal pressure, which drives it to expand rapidly.
(5) The expansion of the bubble allows laser energy to be delivered over a greater distance.

Comparing the results of the two simulations, we find that the difference in bubble shape can be attributed to the duration of phase transition. In the case of the pear-shaped bubble, vaporisation lasts for less than 1 μs. In the case of the elongated bubble, vaporisation continues along the beam direction for over 50 μs. In both cases, the duration of the laser pulse is not a limiting factor. For example, the Ho:YAG laser that generated the pear-shaped bubble has a pulse duration of 70 μs, much longer than the time of vaporisation.

The duration of phase transition can be explained as the result of a race between two bubble growth mechanisms, namely flow advection and the continuation of phase transition. The latter is a unique feature of long-pulse laser-induced cavitation. We hypothesise that at any time instant, if the speed of bubble growth by advection is higher than that by phase transition, the bubble tends to expand spherically. Otherwise, phase transition would occur (or continue), driving the bubble to elongate along the laser beam direction. We have formulated the two speeds using a simplified model problem, and estimated their values for the two experiments using the simulation results. The simulation results support the hypothesis. For example, the speed of bubble growth by phase transition is found to be two orders of magnitude higher in the case of the elongated bubble, whereas the speed of bubble growth by advection is about the same in the two cases. The formulae of bubble growth speeds also indicate possible ways to control the bubble shape, which can be a topic for future studies. For example, assuming the laser's power is fixed, increasing the laser absorption coefficient (e.g. by changing the laser's wavelength) and reducing the laser beam width may facilitate bubble elongation.

The computational model presented in this work is implemented in the M2C code, which is open-source under the GPLv3 license (Wang *et al.* 2021). For example, the models of laser radiation (§ 2.3) and phase transition (§ 2.4) are implemented mostly in LASERABSORPTIONSOLVER.H/CPP and PHASETRANSITION.H, respectively. Finally, it is noteworthy that while the simulations revealed some interesting flow features inside the initial vapour bubble (see e.g. the last row of figure 9), these results have not been validated against laboratory experiments. Accurately measuring flow states inside a small cavitation bubble is challenging, and thus, this work is left for future research.

Funding. The authors gratefully acknowledge the support of the National Science Foundation (NSF) under award CBET-1751487, the support of the Office of Naval Research (ONR) under award N00014-19-1-2102, and the support of the National Institutes of Health (NIH) under awards 2R01-DK052985-26 and

1P20-DK135107-02. Gaoming Xiang also acknowledges the support from the Qilu Young Scholar program (62460082363371) of Shandong University.

Declaration of interests. The authors report no conflict of interest.

Author ORCIDs.
Xuning Zhao https://orcid.org/0000-0001-8019-0999;
Gaoming Xiang https://orcid.org/0000-0002-3789-1789;
Kevin Wang https://orcid.org/0000-0003-1924-4075.

References

Asshauer, T., Rink, K. & Delacretaz, G. 1994 Acoustic transient generation by holmium-laser-induced cavitation bubbles. *J. Appl. Phys.* **76** (9), 5007–5013.

Blackmon, R.L., Irby, P.B. & Fried, N.M. 2010 Holmium:YAG ($\lambda = 2120$ nm) versus thulium fiber ($\lambda = 1908$ nm) laser lithotripsy. *Laser. Surg. Med.* **42** (3), 232–236.

Brennen, C.E. 2014 *Cavitation and Bubble Dynamics*. Cambridge University Press.

Brujan, E.-A., Nahen, K., Schmidt, P. & Vogel, A. 2001 Dynamics of laser-induced cavitation bubbles near an elastic boundary. *J. Fluid Mech.* **433**, 251–281.

Byun, K.-T. & Kwak, H.-Y. 2004 A model of laser-induced cavitation. *Jpn. J. Appl. Phys.* **43** (2R), 621.

Cao, S., Main, A. & Wang, K.G. 2018 Robin-Neumann transmission conditions for fluid-structure coupling: embedded boundary implementation and parameter analysis. *Intl J. Numer. Meth. Engng* **115** (5), 578–603.

Cao, S., Wang, G., Coutier-Delgosha, O. & Wang, K. 2021*a* Shock-induced bubble collapse near solid materials: effect of acoustic impedance. *J. Fluid Mech.* **907**, A17.

Cao, S., Wang, G. & Wang, K.G. 2021*b* A spatially varying Robin interface condition for fluid-structure coupled simulations. *Intl J. Numer. Meth. Engng* **122** (19), 5176–5203.

Chen, J., Ho, D.S., Xiang, G., Sankin, G., Preminger, G.M., Lipkin, M.E. & Zhong, P. 2022 Cavitation plays a vital role in stone dusting during short pulse holmium:YAG laser lithotripsy. *J. Endourol.* **36** (5), 674–683.

Chida, I., Okazaki, K., Shima, S., Kurihara, K., Yuguchi, Y. & Sato, I. 2003 Underwater cutting technology of thick stainless steel with YAG laser. In *First International Symposium on High-Power Laser Macroprocessing*, vol. 4831, pp. 453–458. SPIE.

Choubey, A., Jain, R.K., Ali, S., Singh, R., Vishwakarma, S.C., Agrawal, D.K., Arya, R., Kaul, R., Upadhyaya, B.N. & Oak, S.M. 2015 Studies on pulsed Nd:YAG laser cutting of thick stainless steel in dry air and underwater environment for dismantling applications. *Opt. Laser Technol.* **71**, 6–15.

Dijkink, R. & Ohl, C.-D. 2008 Laser-induced cavitation based micropump. *Lab on a Chip* **8** (10), 1676–1681.

Dular, M. & Coutier-Delgosha, O. 2013 Thermodynamic effects during growth and collapse of a single cavitation bubble. *J. Fluid Mech.* **736**, 44–66.

Faghri, A. & Zhang, Y. 2006 *Transport Phenomena in Multiphase Systems*. Elsevier.

Farhat, C., Gerbeau, J.-F. & Rallu, A. 2012 FIVER: a finite volume method based on exact two-phase Riemann problems and sparse grids for multi-material flows with large density jumps. *J. Comput. Phys.* **231** (19), 6360–6379.

Fried, N.M. 2018 Recent advances in infrared laser lithotripsy. *Biomed. Opt. Express* **9** (9), 4552–4568.

Fried, N.M. & Irby, P.B. 2018 Advances in laser technology and fibre-optic delivery systems in lithotripsy. *Nat. Rev. Urol.* **15** (9), 563–573.

Hardy, L.A., Kennedy, J.D., Wilson, C.R., Irby, P.B. & Fried, N.M. 2016 Cavitation bubble dynamics during thulium fiber laser lithotripsy. In *Photonic Therapeutics and Diagnostics XII*, vol. 9689, pp. 146–151. SPIE.

Ho, D.S., *et al.* 2021 The role of cavitation in energy delivery and stone damage during laser lithotripsy. *J. Endourol.* **35** (6), 860–870.

Howell, J.R., Mengüç, M.P., Daun, K. & Siegel, R. 2020 *Thermal Radiation Heat Transfer*. CRC Press.

Huang, D.Z., De Santis, D. & Farhat, C. 2018 A family of position-and orientation-independent embedded boundary methods for viscous flow and fluid–structure interaction problems. *J. Comput. Phys.* **365**, 74–104.

ISLAM, S.T., MA, W., MICHOPOULOS, J.G. & WANG, K. 2023 Fluid-solid coupled simulation of hypervelocity impact and plasma formation. *Intl J. Impact. Engng* **180**, 104695.

JAIN, R.K., AGRAWAL, D.K., VISHWAKARMA, S.C., CHOUBEY, A.K., UPADHYAYA, B.N. & OAK, S.M. 2010 Development of underwater laser cutting technique for steel and zircaloy for nuclear applications. *Pramana* **75**, 1253–1258.

JANSEN, E.D., ASSHAUER, T., FRENZ, M., MOTAMEDI, M., DELACRÉTAZ, G. & WELCH, A.J. 1996 Effect of pulse duration on bubble formation and laser-induced pressure waves during holmium laser ablation. *Laser. Surg. Med.* **18** (3), 278–293.

JUHASZ, T., KASTIS, G.A., SUÁREZ, C., BOR, Z. & BRON, W.E. 1996 Time-resolved observations of shock waves and cavitation bubbles generated by femtosecond laser pulses in corneal tissue and water. *Laser. Surg. Med.* **19** (1), 23–31.

KHLIFA, I., COUTIER-DELGOSHA, O., FUZIER, S., VABRE, A. & FEZZAA, K. 2013 Velocity measurements in cavitating flows using fast x-ray imaging. In *Congrés Français de Mécanique*.

KLASEBOER, E., TURANGAN, C., FONG, S.W., LIU, T.G., HUNG, K.C. & KHOO, B.C. 2006 Simulations of pressure pulse–bubble interaction using boundary element method. *Comput. Meth. Appl. Mech. Engng* **195** (33–36), 4287–4302.

KOCH, M., LECHNER, C., REUTER, F., KÖHLER, K., METTIN, R. & LAUTERBORN, W. 2016 Numerical modeling of laser generated cavitation bubbles with the finite volume and volume of fluid method using OpenFOAM. *Comput. Fluids* **126**, 71–90.

LAUTERBORN, W. & VOGEL, A. 2013 Shock wave emission by laser generated bubbles. In *Bubble Dynamics and Shock Waves*, pp. 67–103. Springer.

LE MÉTAYER, O. & SAUREL, R. 2016 The Noble–Abel stiffened-gas equation of state. *Phys. Fluids* **28** (4), 046102.

VAN LEEUWEN, T.G.J.M., JANSEN, E.D., MOTAMEDI, M., WELCH, A.J. & BORST, C. 1993 Bubble formation during pulsed laser ablation: mechanism and implications. In *Laser-Tissue Interaction IV*, vol. 1882, pp. 13–22. SPIE.

MA, W., ZHAO, X., ISLAM, S., NARKHEDE, A. & WANG, K. 2023 Efficient solution of bimaterial Riemann problems for compressible multi-material flow simulations. arXiv:2303.08743.

MAIN, A., ZENG, X., AVERY, P. & FARHAT, C. 2017 An enhanced fiver method for multi-material flow problems with second-order convergence rate. *J. Comput. Phys.* **329**, 141–172.

MODEST, M.F. 2013 *Radiative Heat Transfer*. Academic Press.

MOHAMMADZADEH, M., MERCADO, J.M. & OHL, C.-D. 2015 Bubble dynamics in laser lithotripsy. *J. Phys.: Conf. Ser.* **656**, 012004.

OHL, C.-D., ARORA, M., DIJKINK, R., JANVE, V. & LOHSE, D. 2006 Surface cleaning from laser-induced cavitation bubbles. *Appl. Phys. Lett.* **89** (7), 074102.

PADILLA-MARTINEZ, J.P., BERROSPE-RODRIGUEZ, C., AGUILAR, G., RAMIREZ-SAN-JUAN, J.C. & RAMOS-GARCIA, R. 2014 Optic cavitation with CW lasers: a review. *Phys. Fluids* **26** (12), 122007.

PETKOVŠEK, M. & DULAR, M. 2013 Ir measurements of the thermodynamic effects in cavitating flow. *Intl J. Heat Fluid Flow* **44**, 756–763.

PLESSET, M.S. & PROSPERETTI, A. 1977 Bubble dynamics and cavitation. *Annu. Rev. Fluid Mech.* **9**, 145–185.

POŽAR, T. 2020 Cavitation induced by shock wave focusing in eye-like experimental configurations. *Biomed. Opt. Express* **11** (1), 432–447.

PROSPERETTI, A. & PLESSET, M.S. 1978 Vapour-bubble growth in a superheated liquid. *J. Fluid Mech.* **85** (2), 349–368.

SCHOPPINK, J.J., KRIZEK, J., MOSER, C. & RIVAS, D.F. 2023 Cavitation induced by pulsed and continuous-wave fiber lasers in confinement. *Expl Therm. Fluid Sci.* **146**, 110926.

SONG, W.D., HONG, M.H., LUKYANCHUK, B. & CHONG, T.C. 2004 Laser-induced cavitation bubbles for cleaning of solid surfaces. *J. Appl. Phys.* **95** (6), 2952–2956.

SPARROW, E.M. 2018 *Radiation Heat Transfer*. Routledge.

TOMITA, Y., ROBINSON, P.B., TONG, R.P. & BLAKE, J.R. 2002 Growth and collapse of cavitation bubbles near a curved rigid boundary. *J. Fluid Mech.* **466**, 259–283.

TRAXER, O. & KELLER, E.X. 2020 Thulium fiber laser: the new player for kidney stone treatment? A comparison with holmium:YAG laser. *World J. Urol.* **38**, 1883–1894.

VENTIMIGLIA, E. & TRAXER, O. 2019 What is moses effect: a historical perspective. *J. Endourol.* **33** (5), 353–357.

VOGEL, A., ENGELHARDT, R., BEHNLE, U. & PARLITZ, U. 1996 Minimization of cavitation effects in pulsed laser ablation illustrated on laser angioplasty. *Appl. Phys.* B **62**, 173–182.

VOGEL, A., HENTSCHEL, W., HOLZFUSS, J. & LAUTERBORN, W. 1986 Cavitation bubble dynamics and acoustic transient generation in ocular surgery with pulsed neodymium:YAG lasers. *Ophthalmology* **93** (10), 1259–1269.

WAGNER, W., KRETZSCHMAR, H.-J., SPAN, R. & KRAUSS, R. 2010 D2 properties of selected important pure substances. In *VDI Heat Atlas*. VDI-Buch. Springer.

WANG, K., MA, W., ZHAO, X., ISLAM, S. & NARKHEDE, A. 2021 M2C solver. https://github.com/kevinwgy/m2c.git.

WANG, K.G. 2017 Multiphase fluid-solid coupled analysis of shock-bubble-stone interaction in shockwave lithotripsy. *IntL J. Numer. Meth. Biomed. Engng* **33** (10), e2855.

WARNEZ, M.T. & JOHNSEN, E. 2015 Numerical modeling of bubble dynamics in viscoelastic media with relaxation. *Phys. Fluids* **27** (6), 063103.

WELCH, A.J., VAN GEMERT, M.J.C. 2011 *Optical-Thermal Response of Laser-Irradiated Tissue*, 2nd edn. Springer.

XIANG, G., LI, D., CHEN, J., MISHRA, A., SANKIN, G., ZHAO, X., TANG, Y., WANG, K., YAO, J. & ZHONG, P. 2023 Dissimilar cavitation dynamics and damage patterns produced by parallel fiber alignment to the stone surface in holmium:yttrium aluminum garnet laser lithotripsy. *Phys. Fluids* **35** (3), 033303.

ZEIN, A., HANTKE, M. & WARNECKE, G. 2013 On the modeling and simulation of a laser-induced cavitation bubble. *Intl J. Numer. Meth. Fluids* **73** (2), 172–203.

ZHANG, Y. & PROSPERETTI, A. 2021 Dynamics, heat and mass transfer of a plasmonic bubble on a solid surface. *Intl J. Heat Mass Transfer* **167**, 120814.

ZHAO, X., MA, W. & WANG, K. 2023 Simulating laser–fluid coupling and laser-induced cavitation using embedded boundary and level set methods. *J. Comput. Phys.* **472**, 111656.

ZHONG, X., ESHRAGHI, J., VLACHOS, P., DABIRI, S. & ARDEKANI, A.M. 2020 A model for a laser-induced cavitation bubble. *Intl J. Multiphase Flow* **132**, 103433.

ZWAAN, E., LE GAC, S., TSUJI, K. & OHL, C.-D. 2007 Controlled cavitation in microfluidic systems. *Phys. Rev. Lett.* **98** (25), 254501.